Contributions to Mineralogy and Petrology (2022) 177: 80
https://doi.org/10.1007/s00410-022-01936-3

ORIGINAL PAPER

Newly detected shock-induced high-pressure phases formed in amphibolite clasts of the suevite breccia (Ries impact crater, Germany): Liebermannite, kokchetavite, and other ultrahigh-pressure phases

Volker Stähle[1] · Chutimun Chanmuang N.[2] · Winfried H. Schwarz[1,3] · Mario Trieloff[1,3] · Alexander Varychev[1]

Received: 2 December 2021 / Accepted: 22 June 2022 / Published online: 2 August 2022

Abstract
Amphibolite clasts in the suevite of the Ries impact crater contain shock-induced melt veins (SMVs) with high-pressure phases such as majoritic garnet, jadeitic clinopyroxene and others. In addition, heat conduction from hot SMVs into adjacent rock portions locally produced further high *P–T* melt pools. These melts were preferentially generated in rock domains, where the SMVs cross older ('pre-Ries') veinlets with analcime or prehnite and larger grains of sericitized plagioclase. Melting of such chemically different local bulk systems (Na-, Ca-, Ca-Na- and K-Na-rich) was facilitated by low solidus temperatures of the original secondary OH-bearing phases. From the resulting shock-induced melts, liebermannite, kokchetavite, jadeite, nonstoichiometric and albitic jadeite, grossular, vuagnatite, lawsonite + coesite, and clinozoisite crystallized during pressure release. Vuagnatite is now proven to be a genuine high-pressure phase. Its ubiquitous distance of 20–35 µm from the hot shock veins suggests a temperature sensitivity typical for an OH-bearing phase. In local Na-rich melts albitic jadeite appears instead of the assemblage jadeite + SiO_2. Liebermannite, a dense polymorph of K-feldspar was identified by Raman spectroscopy. After stishovite, liebermannite constitutes the second known high-pressure phase in the Ries that contains silicon exclusively in six-fold coordination. The $KAlSi_3O_8$-polymorph kokchetavite was formed in alkali-rich melt glasses. Pressure and temperature values in the range of about 8–11 GPa and ~ 800–1100 °C were estimated from the chemical compositions of locally occurring majoritic garnets (Si = 3.21–3.32 and 3.06–3.10 apfu), respectively, and the presence of fine-grained aggregates of lawsonite and coesite. Generally, the neighboring areas of the veins are characterized by a sequence of variable high-pressure phases documenting strongly falling *P–T* conditions with increasing distance from the vein. These novel features enlighten the dynamic event during passage of a shock wave.

Keywords Ries impact crater · Shock vein · Liebermannite · Kokchetavite · Jadeite · Vuagnatite · Lawsonite

Introduction

Shock-induced melt veins (SMVs) in natural crystalline rocks got much attention by Earth scientists in the past three decades. The existence of a large variety of shock-induced high-pressure phases within or adjacent to thin shock-melt veins allows an assessment for the high pressure (*P*) and temperature (*T*) conditions of their formation. The occurrence of such phases in shocked crystalline rocks is linked to the passage of supersonic shock waves that are produced by impacts of asteroids or meteorites on planetary or terrestrial surfaces. It is worth mentioning that SMVs with many high-pressure phases contribute to the set of parameters of specific shock-related effects that were originally described

Communicated by Othmar Müntener.

✉ Winfried H. Schwarz
Winfried.Schwarz@geow.uni-heidelberg.de

[1] Institute of Earth Sciences, Heidelberg University, Im Neuenheimer Feld 234–236, 69120 Heidelberg, Germany

[2] Institut für Mineralogie und Kristallographie, Universität Wien, Althanstr. 14, 1090 Vienna, Austria

[3] Klaus-Tschira-Labor für Kosmochemie, Heidelberg University, Im Neuenheimer Feld 234–236, 69120 Heidelberg, Germany

under the terms 'shock metamorphism' or 'impact metamorphism' (e.g. Chao 1967, 1968; French and Short 1968; von Engelhardt and Stöffler 1968; Robertson et al. 1968; Stöffler 1972; Stöffler and Grieve 2007; French 1998; Langenhorst 2002; French and Koeberl 2010; Langenhorst and Deutsch 2012).

Shock-melt veins usually form an 'erratic' interlocking network of former melt films or may occur along older rock fractures that may be filled with late-stage hydrothermal minerals (e.g. Stähle et al. 2017). Small-scale offsets of mineral fragments or small lateral displacements of crossing pre-shock veinlets point to slip movements under high pressures producing melt films at very high temperatures of > 2000 °C. Such SMVs form immediately at the beginning of the contact/compression stage (Melosh 1989, 2013; French 1998) during evolution of an impact structure. By passing through rocks and minerals with varying seismic impedance contrasts (*shock wave velocity* × *mineral density*) the original plane shock-front becomes distorted and convoluted. Within dense minerals or tight crystalline rocks, the shock wave travels faster than in less dense minerals or in porous rocks. The complex interaction of shock waves with crystalline rocks and minerals locally lead to shear stresses and frictional melting in a complex slip system wherein SMVs are created (Kenkmann et al. 2000; Heider and Kenkmann 2003; Sharp and DeCarli 2006; Spray 2010; Ogilvie et al. 2011; Walton et al. 2016). Detailed models for the formation of SMVs in naturally shocked rocks are given in Walton et al. (2016) and Spray and Boonsue (2018).

Most findings on SMVs and their accompanying high-pressure phase assemblages came from studies on meteorite samples (e.g. Stöffler et al. 1991; Tomioka and Miyahara 2017). High-pressure phase equilibria in adequate chemical systems determined by static high-pressure experiments allow well-grounded estimations of the prevailing *P–T-t* conditions (*t* = time) under dynamic shock compression (Chen et al. 1996; Langenhorst and Poirier 2000a, b; Beck et al. 2005; Ohtani et al. 2004; Sharp and DeCarli 2006; Xie et al. 2006; Gillet et al. 2007; Tschauner et al. 2014; Ma et al. 2016; Tomioka and Miyahara 2017; Sharp et al. 2019; Hu and Sharp 2022). Beyond that, the shock-induced high-pressure phases also give substantial indications for the mineralogical composition of the Earth's upper mantle and transition zone.

For several terrestrial impact craters such as Vredefort in South Africa (Martini 1978, 1991; Spray and Boonsue 2018), Manicouagan in Canada (Biren and Spray 2011; Boonsue and Spray 2017, Steen River in Canada (Walton et al. 2016, 2018), Sudbury in Canada (Thompson and Spray 1996), and the Ries in Germany (Dressler and Graup 1970; Stähle et al. 2011, 2017; Tschauner et al. 2020a, b; Ma et al. 2022), SMVs within various crystalline rocks have been recorded. In the Ries impact structure, such veins mostly occur in moderately shocked suevite clasts. The variability of shocked basement rocks within several suevite occurrences scattered around the Ries crater was reported by von Engelhardt (1997). A detailed report with a chronological recovering of recently discovered shock-induced high-pressure phases in both terrestrial and extraterrestrial rocks is given by Miyahara et al. (2021).

This study deals with two amphibolite clasts that were chosen from a larger suite of SMV-bearing crystalline rocks from the Ries suevite (Stähle et al. 2011, 2017). Both clasts are relatively coarse-grained and are cut by several thin SMVs that partially traverse pre-shock hydrothermal veinlets of variable compositions. Moreover, broader SMVs are often surrounded by neighboring areas that were apparently shocked at lower *P–T* conditions than the veins, leading to different shock-induced mineral associations despite similar bulk compositions of both domains (Sharp and DeCarli 2006). A representative example for such a situation in the Ries impact crater is shown by the transformation of a chloritized former biotite grain that is in direct contact with a SMV rich in majoritic garnet. With increasing distance from this SMV, majoritic garnet changes its composition and finally grades into normal silicate garnet with tiny magnetite inclusions due to spatially declining *P–T* conditions (Stähle et al. 2017: Fig. 2c, d). Another instructive example is the transformation of quartz to stishovite in contact with a SMV (Stähle et al. 2017: Fig. 2e). A preferred formation of stishovite adjacent to shock veins is also known from the Vredefort impact crater (Spray and Boonsue 2018).

The prime goal of this paper was to demonstrate how small-scale variations in primary bulk composition will influence the shock-induced mineralogy not only within the SMV but also within its immediate neighborhood. It is well known that shock veins predominantly cool via thermal conduction affecting adjacent volumes (Sharp and DeCarli 2006; Xie et al. 2006). Using a multitude of dense mineral phases that were found for the first time in the Ries impact structure, we estimate *P–T* conditions by applying results from high pressure phase equilibria. The high-pressure-induced formations adjacent of SMVs will be treated as visual fingerprints of a shock wave that started firstly from the central point of the Ries impact.

Geologic background

The circular ~ 25 km-wide Ries impact crater in Southern Germany is one of the places on Earth where shock-induced melt veins were found in clasts trapped in suevite (Stähle et al. 2011, 2017). The rather young age of this structure (c. 14.8 Ma; Buchner et al. 2013; Schwarz and Lippolt 2014; Schmieder et al. 2018; Schwarz et al. 2020) favored the preservation of a thick central fallback deposit and a far-reaching ejecta blanket outside the crater. An overview on the geology

of the target rocks as well as the crater-fill and ejecta deposits along with some geophysical data is given by Pohl et al. (1977) and Stöffler et al. (2013). The occurrence, stratigraphy, and composition of all existing lithological units can be studied in detail in several well documented outcrops (Schmidt-Kaler et al.1970; Chao et al. 1978; Hüttner and Schmidt-Kaler 1999).

The target rocks at the Ries impact structure consisted of a flat-lying sequence of Permian to Mesozoic sedimentary rocks that unconformably overlie a Variscan crystalline basement. The suevite contains a variety of Variscan crystalline bedrocks such as biotite-plagioclase gneisses, garnet-cordierite-sillimanite gneisses, amphibolites, and granites (Dressler et al. 1969; Graup 1978). Like everywhere in western Europe, these crystalline rocks show a widespread episodic hydrothermal overprint that took place in 'pre-Ries' times (Late Jurassic to Tertiary) (e.g. Lippolt and Kirsch 1994; Schlegel et al. 2007; Brockamp et al. 2015). This overprint resulted in a strong sericitization of Ca-rich plagioclase domains, the local chloritization of biotite and amphibole, and the formation of veinlets of analcime or prehnite.

Sampling and analytical techniques

The two investigated amphibolite clasts (ZLN141 and ZLN128/128a) were taken from the suevite of Zipplingen that represents a local high-temperature ejecta in the NW part of the Nördlinger Ries (Stähle et al. 2011, 2017). High-quality polished thin sections of the two amphibolite clasts were studied in transmitted and reflected light.

For determination of micro-textures, back-scattered electron (BSE) images were obtained using a LEO 440 scanning electron microscope (SEM) at the Institute of Earth Sciences, Heidelberg University. This instrument is equipped with an X-Max 80 mm^2 silicon-drift detector (SDD) and the INCA energy software from Oxford Instruments (https://www.brandonu.ca/microscope/files/2010/08/pdf_3.pdf). For quantitative energy-dispersive X-ray EDX analyses (EDXA), the operating conditions were 20 kV accelerating voltage, 1–2 µm beam diameter, and 1.8 nA sample current. Quantitative calibration check was done with cobalt.

Electron microprobe analyses (EMPA) of silicate and oxide phases were obtained using a CAMECA SX51 instrument equipped with five wavelength-dispersive spectrometers (Institute of Earth Sciences, Heidelberg University). Operating parameters were 15 kV accelerating voltage, 20 nA beam current, ~ 1 µm beam size, and counting times of 30 s for Al and Ca, 20 s for Ti and 10 s for all other elements. Mineral and synthetic silicate and oxide reference materials were used for calibration, namely wollastonite for Ca and Si, rhodonite for Mn, albite for Na, anorthite for Ca, orthoclase for K, anorthite for Al, Fe_2O_3 for Fe, Cr_2O_3 for Cr, TiO_2 for Ti and MgO for Mg. Raw data were corrected for matrix effects with the PAP algorithm implemented by CAMECA. Detection limits were 0.04 wt% SiO_2, 0.06 wt% TiO_2, 0.04 wt% Al_2O_3, 0.07 wt% Cr_2O_3, 0.11 wt% FeO, 0.08 wt% MnO, 0.07 wt% MgO, 0.04 wt% CaO, 0.03 wt% Na_2O and 0.03 wt% K_2O. The total analytical error is < 1% relative.

Raman spectra of various small-sized mineral phases were obtained with point measurements by means of a Horiba LabRAM Evolution spectrometer system at the Institute of Mineralogy and Crystallography at the University of Vienna. This confocal, edge filter-based Raman microprobe system (focal length 800 mm) is equipped with an Olympus BX41 optical microscope and a Peltier-cooled charge-coupled device (CCD) detector. Spectra were obtained by excitation using a 532-nm emission of frequency-doubled Nd:YAG laser (10 mW behind the objective). With the Olympus 100 × objective lens (numerical aperture 0.9), the focal spot was ~ 1 µm in diameter. The spectrometer was operated in the confocal mode; the real volume resolution is assessed to be better than 1 µm laterally and 2–3 µm in depth. A diffraction grating with 1800 grooves per mm was used to disperse the scattered light. The wavenumber accuracy (calibrated using Ne lamp emissions) was 0.5 cm^{-1} and the spectral resolution was 1.0 cm^{-1}. For further details see Nasdala et al. (2018).

Results

Petrography of amphibolite clasts

The weakly to moderately shocked amphibolite clasts in the suevite measure about 5–10 cm in diameter and have brownish to green colors. Polished thin sections are shown in transmitted light photographs (Fig. 1a–c). Both rocks are coarse-grained and their primary minerals are magnesio-hornblende, plagioclase, and minor biotite, while the phases apatite, zircon, and magnetite are accessory. The average grain size of these rocks (~ 2 mm) is relatively large in relation to the thickness of their SMVs (< 1.1 mm) that partially traverse 'pre-Ries' veinlets of either analcime or prehnite. Moreover, the SMVs also traverse larger hornblende grains as well as strongly sericitized former Ca-rich plagioclase domains. This situation results in chemically different local subsystems, such as Na-rich (former analcime), Ca-rich (former prehnite), Na-Ca-rich (former plagioclase), K-Na-rich (sericitized plagioclase), and Mg–Fe–Ca–Na–rich (amphibole), that are expected to produce variable mineral parageneses during shock metamorphism at variable *P–T* conditions.

Most SMVs contain µm-sized grains of majoritic garnet with variable amounts of Si, Al, Fe, Mg, Ca, K, and Na (Stähle et al. 2011, 2017). Their chemical compositions yielded high crystallization pressures of 16.7 ± 0.5 GPa for ZLN128 and 16.5 ± 1.3 GPa for ZLN141, using

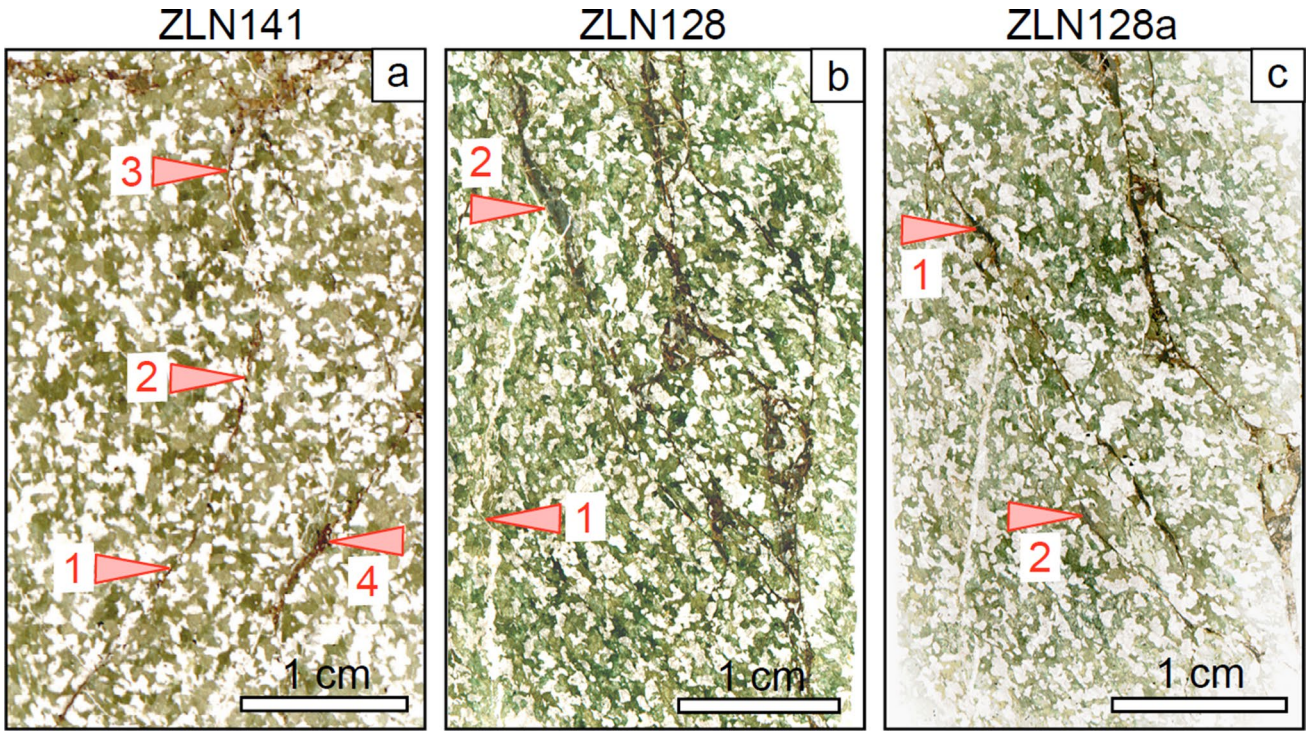

Fig. 1 Thin sections of suevite clasts of amphibolite-containing shock-induced veins in plane polarized light (PPL). **a** ZLN141 shows various shock veins running in different directions. The near-vertical vein in the middle of ZLN141 runs predominantly along a preexisting analcime veinlet (between the two red arrows 1 and 2). In the lower left corner of the figure, another 'NW–SE' running analcime veinlet (white) indicates a right-lateral slip movement (~900 µm offset) along the brownish shock vein. At arrow 3, the shock vein consists of an amphibolitic melt where omphacitic jadeite crystallized. In the SMV at arrow 4 liebermannite was found within a clast of DPG. **b** ZLN128 shows a bunch of broader shock veins, which run predominantly from the upper left to the lower right. A colorless, ~ 300 µm-thick prehnite veinlet is visible at the left side of the amphibolite thin section. This veinlet is cut by shock veins (red arrow 2). At arrow 1, a thin analcime veinlet indicates a left-lateral movement. **c** ZLN128a shows a triple of shock veins. The upper arrow 1 points to an area where Na–K-rich melt glass with assemblages of liebermannite + kokchetavite and albitic jadeite occurs, and the lower arrow 2 points to a place where crystallizations of vuagnatite + grossular and lawsonite + coesite from a Ca-rich diaplectic plagioclase glass were found

the geobarometer of Wijbrans et al. (2016) that is based on experiments.

Sample ZLN141

The non-foliated amphibolite ZLN141 contains approximately equal amounts of brownish green magnesio-hornblende and former plagioclase that is completely transformed to diaplectic plagioclase glass (DPG) with nearly constant compositions of $Ab_{49–42}An_{47–55}Or_{01–02}$ (Fig. 1a; Table 1). Magnesio-hornblende (Hawthorne et al. 2012) is heavily shattered and shows the average chemical formula $^{A}(K_{0.14}Na_{0.32})^{M4}(Na_{0.09}Ca_{1.91})^{M1–M3}(Mg_{2.59}Mn_{0.04}Fe^{2+}_{1.31}Fe^{3+}_{0.56}Ti_{0.14}Al_{0.36})^{T}(Al_{1.47}Si_{6.53})O_{22}(OH)_2$ (Table 1), whereby $Fe^{3+}/(Fe^{2+}+Fe^{3+})$ is assumed to be 0.3 as usual in high-grade amphibolite. Most plagioclase grains are completely shock-transformed to diaplectic glass (DPG, Table 1). Due to these features, sample ZLN141 is classified into shock stage M-S4 (Stöffler et al. 2018). In transmitted light, many DPG grains outside and within the SMVs locally appear dusty due to the occurrence of numerous small sericite flakes that are unevenly distributed. In addition, some biotite grains are secondarily replaced by fine-grained chlorite and Ti–rich secondary minerals.

A special feature of sample ZLN141 is the presence of thin hydrothermal analcime veinlets that were formed along faults, as indicated by broken fragments of hornblende that are 'floating' in an isotropic matrix of analcime (Fig. 2a, green arrow). In the studied thin section, three branches of SMVs are visible (Fig. 1a). A long, near-vertical vein (marked with red arrows 1, 2, 3) merges into a horizontal vein at the top of the section. The third vein runs diagonally through the lower right part of the section (Fig. 1a, red arrow 4). Between the points marked by the red arrows 1 and 2, the first SMV mostly runs within an older analcime veinlet. The shock-induced minerals in this analcime-dominated part

Table 1 Electron microprobe analyses (EMPA) and energy-dispersive X-ray analyses (EDXA) of primary minerals and shock-induced glasses and phengite

Mineral	Mhb	Mhb	Mhb	Prh	Prh	DPG	DPG	DPG	DPG	Mc	Mc	AMG	AMG	Ms	Ph
Method	EMPA	EDXA	EMPA	EMPA	EDXA	EMPA	EMPA	EMPA	EMPA	EDXA	EDXA	EMPA	EMPA	EMPA	EMPA
Analysis#	128a-28	128a-52	141–227	128–56	128–8	141–02	141–203	128a-36	128a-15	128a-11	128a-12	128–80	Ave (8)	128a-41	128–99
SiO_2	45.12	45.96	44.19	44.72	44.43	55.06	55.49	50.42	49.60	65.22	64.90	69.05	67.43	47.49	51.20
TiO_2	1.28	1.20	1.30	0.01	0.00	0.00	0.00	0.01	0.00	0.00	0.00	0.00	0.00	0.00	0.04
Al_2O_3	10.05	10.51	10.50	23.79	23.80	28.51	28.37	32.15	31.95	17.83	18.01	20.61	21.16	36.76	28.80
Cr_2O_3	0.07	0.00	0.02	0.00	0.00	0.03	0.00	0.03	0.00	0.00	0.00	0.07	0.02	0.00	0.08
Fe_2O_3	4.48	4.49	4.95	0.21	0.22	0.00	0.00	0.00	0.00	0.37	0.46	0.00	0.00	0.59	0.00
FeO	10.45	9.44	10.40	0.00	0.00	0.19	0.16	0.17	0.21	0.00	0.00	0.09	0.11	0.00	2.36
MnO	0.21	0.20	0.29	0.00	0.00	0.03	0.00	0.03	0.00	0.00	0.00	0.03	0.02	0.04	0.00
MgO	12.56	12.96	11.73	0.00	0.19	0.00	0.00	0.00	0.00	0.10	0.11	0.00	0.07	0.20	2.03
CaO	11.45	11.04	12.10	26.12	27.07	11.29	9.75	14.61	15.21	0.45	0.35	1.23	1.82	0.16	0.41
Na_2O	1.40	1.54	1.41	0.28	0.28	4.86	5.27	2.40	2.90	1.23	1.12	4.93	5.50	0.23	0.11
K_2O	0.57	0.61	0.76	0.02	0.07	0.15	0.29	0.10	0.07	14.28	14.54	3.53	3.48	10.04	9.96
H_2O*	2.05	2.07	2.03	4.36	4.38	–	–	–	–	–	–	–	–	4.57	4.51
Total	100.19	100.02	99.68	99.46	100.44	100.12	99.93	99.92	99.94	99.48	99.49	99.54	99.64	100.08	99.50
Number of cations (apfu)															
Si	6.599	6.671	6.525	3.075	3.040	2.480	2.508	2.293	2.267	3.010	3.000			3.114	3.404
Ti	0.141	0.131	0.144	0.001	0.000	0.000	0.000	0.000	0.000	0.000	0.000			0.000	0.002
Al	1.732	1.798	1.827	1.928	1.919	1.513	1.511	1.723	1.721	0.970	0.981			2.841	2.257
Cr	0.008	0.000	0.002	0.000	0.000	0.001	0.000	0.001	0.000	0.000	0.000			0.000	0.004
Fe^{3+}	0.548	0.491	0.550	0.011	0.011	0.000	0.000	0.000	0.000	0.013	0.016			0.030	0.009
Fe^{2+}	1.278	1.145	1.284	0.000	0.000	0.007	0.006	0.006	0.008	0.000	0.000			0.000	0.122
Mn	0.026	0.025	0.036	0.000	0.000	0.001	0.000	0.001	0.000	0.000	0.000			0.002	0.000
Mg	2.738	2.804	2.582	0.000	0.019	0.000	0.000	0.000	0.000	0.007	0.008			0.020	0.201
Ca	1.794	1.717	1.914	1.924	1.984	0.545	0.472	0.712	0.745	0.022	0.017			0.011	0.029
Na	0.397	0.433	0.404	0.031	0.037	0.424	0.461	0.212	0.257	0.110	0.101			0.029	0.014
K	0.106	0.133	0.143	0.002	0.006	0.009	0.017	0.006	0.004	0.841	0.857			0.840	0.845
Total	15.367	15.348	15.411	6.972	7.016	4.980	4.975	4.954	5.002	4.973	4.980			6.887	6.887

Formulae are based on 22 oxygen anions and 2 OH^- for amphibole (Mhb), 10 oxygen anions and 2 OH^- for prehnite (Prh), 8 oxygen anions for diaplectic plagioclase glass (DPG) and microcline-perthite (Mc), and 10 oxygen anions and 2 OH^- for muscovite (Ms) and shock-metamorphic phengite (Ph). No formulae were calculated for alkaline melt glass (AMG).

*H_2O** calculated water content, *Ave (8)* average of 8 analyses

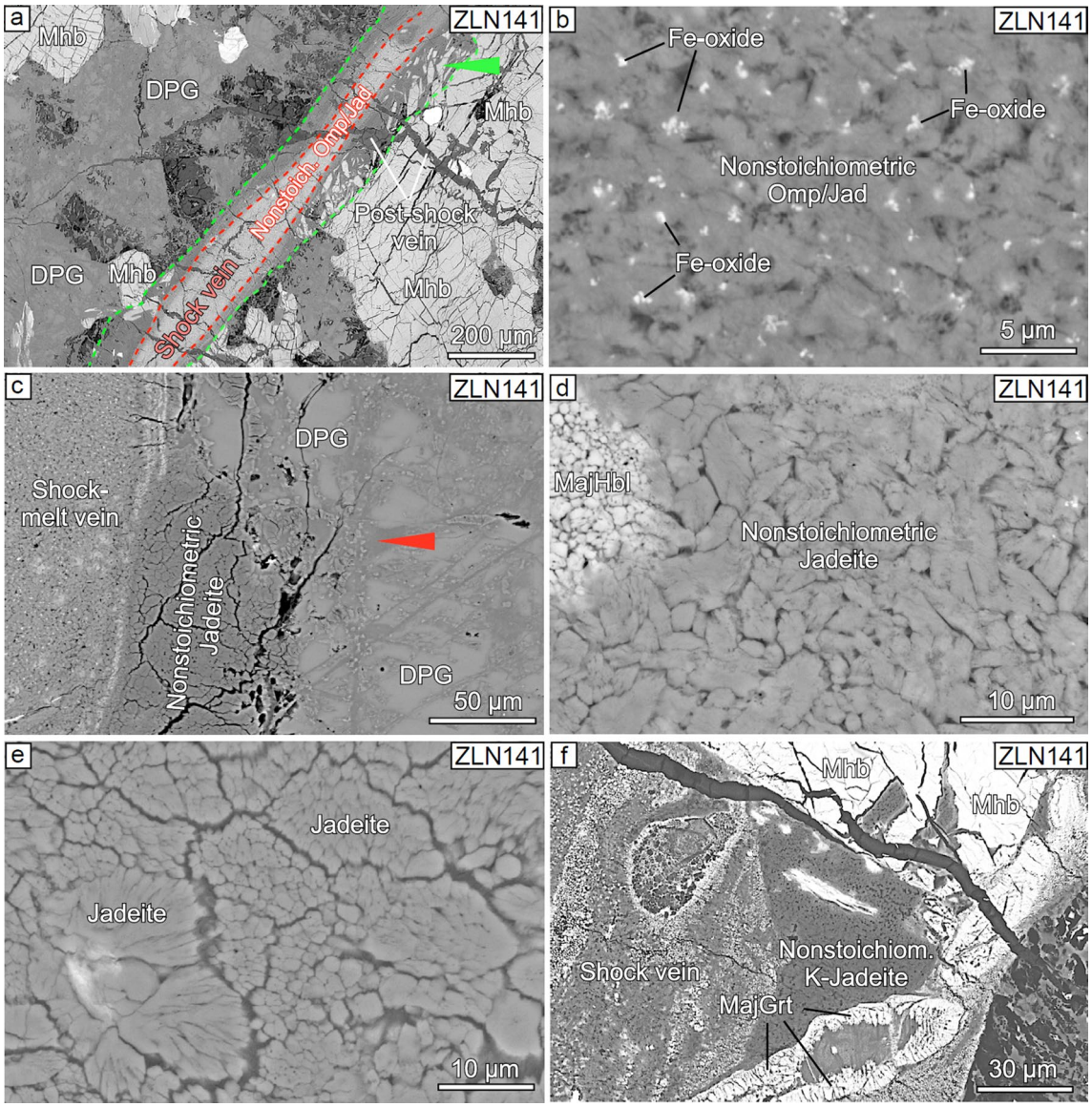

Fig. 2 BSE images of high-pressure phases within and adjacent to a single shock vein that developed predominantly within a pre-existing analcime veinlet (ZLN141). **a** A shock vein (red dashed lines) with nonstoichiometric omphacitic jadeite (Omp/Jad) runs within the older analcime veinlet (green dashed lines). Note the fragments of magnesio-hornblende in a matrix of analcime (green arrow). A post-shock vein filled with montmorillonite traverses the shock vein. DPG = diaplectic plagioclase glass; Mhb = magnesio-hornblende. **b** Close-up of nonstoichiometric omphacite/jadeite with isolated grains of an Fe-Oxide within the shock vein. **c** Border area of a shock melt vein (left) and a large grain of diaplectic plagioclase glass (DPG) on the right side. Between both, a volume of shock-induced grains of nonstoichiometric jadeite occurs. The DPG grain contains darker zones of shock-induced Na-Si-rich melt (red arrow). **d** Close-up of nonstoichiometric jadeite grains occurring outside the wall of a shock vein (compare Fig. 2c). At the left the breakdown of hornblende to light grains of majoritic garnet (MajHbl) is perceptible. **e** Close-up of radiating aggregations of elongated jadeite crystals. **f** Within the central part of the image, K-bearing nonstoichiometric K-jadeite grains assembled within a former grain of sericitized plagioclase are visible. On the left side of the image, the shock vein is seen with aggregations of majoritic garnet (bright) and nonstoichiometric omphacitic jadeite (darker gray). The longish former grain at the lower side is a majoritized hornblende grain with a fused core as described in Stähle et al. (2017)

of the vein deviate from those of ordinary majoritic garnet-bearing SMVs.

Sample ZLN128/128a

Both thin sections were taken from different parts of the clast. The medium-grained amphibolite is nearly isotropic and shows interlocking grains of amphibole and grayish-white plagioclase (Fig. 1b, c; Table 1). The SMVs

in this sample display large variabilities in cross-section (~ 10–1100 µm) and include some lithic clasts. Amphibole grains are locally heavily shattered and results of EMPA (Table 1) give the approximate formula $^{A}(K_{0.11}Na_{0.19})^{M4}(Na_{0.21}Ca_{1.79})^{M1-M3}(Mg_{2.75}Mn_{0.03}Fe^{2+}_{1.30}Fe^{3+}_{0.57}Cr_{0.01}Al_{0.34})^{T}(Al_{1.40}Si_{6.60})\ O_{22}(OH)_2$ that corresponds to magnesio-hornblende (Hawthorne et al. 2012). Smaller hornblende fragments within the veins are completely shock-transformed to red-brown colored (transmitted light) majoritic garnet (Stähle et al. 2011: Fig. 2).

Plagioclase grains within and near to the SMVs are transformed to DPG ($Ab_{22-26}An_{71-75}Or_{<01}$), while those located at larger distances from SMVs still are birefringent. These characteristics permit the classification of this sample into shock stage M-S3 to M-S4 after Stöffler et al. (2018). Like in sample ZL141, plagioclase underwent a 'pre-Ries' partial transformation to sericite. Very rarely, larger grains of microcline occur. Late- to post-Variscan ('pre-Ries') veinlets of prehnite and analcime can easily be seen (Fig. 1b, c; Table 1).

Na-rich shock vein within a pre-existing analcime veinlet

One SMV in ZLN141 invaded into an analcime veinlet and runs longitudinally along its center (Fig. 1a, between arrowheads 1 and 2). Within the veinlet, the observed SMV swells up and down and runs off sporadically. Upwards from arrowhead 3, the contents of this SMV are essentially derived from both amphibole and intermediate plagioclase. In such a 'normal' case of a more metabasaltic vein composition, majoritic garnet is the dominant phase (Stähle et al. 2017). However, in areas where the SMV runs within the former analcime veinlet and/or plagioclase, its chemical bulk composition becomes lowered in Fe, Mg, and Ca, but increased in Na, resulting in crystals of nonstoichiometric omphacitic jadeite (Fig. 2b; Table 2). The chemical compositions of these pyroxene crystals obtained by EMPA suggest the presence of significant M2-vacancies of 0.17–0.23, while Si ≈ 2.0 apfu (Table 2). Following McCormick (1986), we call such pyroxenes 'nonstoichiometric'. This name, however, should not be mistaken with the name 'albitic jadeite' that is characterized by both, significant M2-vacanies (~ 0.25 apfu) and considerable ^{VI}Si contents ($^{IV}Si + {}^{VI}Si \approx 2.2$ apfu), and occurs in recrystallized DPGs (Ma et al. 2022). The Raman spectrum of this nonstoichiometric omphacitic jadeite shows relatively broad peaks (Fig. 3a) that may result from a reduction in phonon-life time, caused by the vacancy at M2. However, it seems that one cannot completely rely on Raman spectra in assessing nonstoichiometric Cpx (Baziotis et al. 2022). The positions of the two main Raman peaks at 365 cm^{-1} and 687 cm^{-1} (Fig. 3a) are typical for relatively Omp-rich jadeite (e.g. Wang et al. 2001). This pyroxene is locally accompanied by small, isolated grains of an Fe-oxide phase (Fig. 2b). Due to the small grain size of these particles (< 1 µm), we were not able to quantitatively analyze this phase. However, recent high-pressure experiments on the FeO-Fe_3O_4 system revealed that at pressures above about 8–9 GPa two other phases, namely Fe_4O_5 and Fe_5O_6, exist, whereby at constant *P* and *T*, but moderately increasing f_{O2}, wüstite ($Fe_{1-x}O$) is followed by Fe_5O_6 and then Fe_4O_5 and still later Fe_2O_3 (Lavina et al. 2011; Lavina and Meng 2015; Myhill et al. 2016; Hikosaka et al. 2019; Woodland et al. 2022).

The Raman spectrum of altered analcime ($Na_{16}[Al_{16}Si_{32}O_{96}]\cdot 16H_2O$) (Fig. 3b) was taken just outside the SMV (Fig. 2a) within a crossing thin veinlet of analcime. Although the main peak at 483 cm^{-1} corresponds to four analcime spectra in the RRUFF database, the form of this peak in our case is strongly broadened and asymmetric, and, therefore, it covers two smaller peaks at ~ 296 and ~ 385 cm^{-1}. Moreover, the peak at ~ 1101 cm^{-1} is also remarkably broad and asymmetric. In addition, the intensity ratio of the 483 cm^{-1} peak to the 1101 cm^{-1} peak in our spectrum is clearly lower than that in all RRUFF Raman spectra. These differences between the Raman spectrum types may be caused by incomplete structural changes of the Si/Al distribution in the framework, a loss of H_2O molecules or an incomplete transformation to an amorphous phase. At low-pressure values (< 1.1 GPa) the cubic or slightly tetragonal or orthorhombic forms of analcime are stable. At ~ 1.1 GPa there is a first-order phase transition to the triclinic form of analcime that is stable at higher pressure. While the cubic low-*P* form is characterized by a fully disordered Si/Al distribution in the 4- and 6-membered rings, the trigonal high-*P* form is characterized by a tilting of (Si,Al)-tetrahedra and a deformation of all tetrahedral rings. There may also be a more ordered distribution of Si and Al (Gatta et al. 2006; Likhacheva et al. 2012; Gatta and Lee 2014). The width of both Raman peaks 483 cm^{-1} and 1101 cm^{-1} (Fig. 3b) seems to indicate that analcime grains near to SMVs were at least partially in a 'glassy' state.

Along the outer walls on both sides of the SMV, domains with lathy crystals of nonstoichiometric jadeite occur (Fig. 2c, d). In Fig. 2d, the contact of such pyroxene grains with majoritized hornblende is shown on the left. The Raman spectrum of these pyroxene grains shows main peaks at 695 cm^{-1} and 370 cm^{-1} (Fig. 3c), and such values are typical for jadeite with a small omphacite component (Wang et al. 2001). Microprobe analyses showed that these crystals are nonstoichiometric with a vacancy of ~ 0.23 at the M2 site (Table 2).

More remote from the SMV with nonstoichiometric omphacitic jadeite (Fig. 2b), aggregates of jadeite sheaves occur (Fig. 2e). The sizes and radiating textures of these crystals are exceptional. These jadeite grains are nearly

Table 2 Electron microprobe analyses (EMPA) and energy-dispersive X-ray analyses (EDXA) of clinopyroxene types in samples ZLN141 and ZLN128a

Mineral	Nonstoichiometric Omp/Jad			Nonstoichiometric Jadeite			Jadeite	Jadeite	Jadeite	Nonstoichiometric K-Jadeite			Albitic Jadeite		
Method	EMPA	EMPA	EMPA	EMPA	EMPA	EMPA	EMPA	EMPA	EMPA	EMPA	EMPA	EMPA	EDXA	EDXA	EDXA
Analysis#	141–01	141–03	Ave (6)	141–07	141–08	Ave (5)	141–14	141–240	Ave (8)	141–37	141–40	Ave (5)	128a-29	128a-21	Ave (8)
SiO_2	57.09	58.38	58.55	61.50	60.73	61.31	60.03	60.33	60.33	60.16	61.23	60.87	65.97	66.05	65.89
TiO_2	0.36	0.36	0.41	0.09	0.00	0.04	0.00	0.00	0.00	0.15	0.07	0.06	0.00	0.11	0.01
Al_2O_3	21.98	19.74	21.99	25.95	26.22	25.56	25.34	25.48	24.58	25.57	26.36	25.68	20.09	19.81	20.23
Cr_2O_3	0.00	0.14	0.01	0.00	0.02	0.00	0.09	0.00	0.01	0.01	0.00	0.01	0.00	0.00	0.00
Fe_2O_3	0.00	0.00	0.00	0.00	0.00	0.00	0.00	0.00	0.00	0.00	0.00	0.00	0.00	0.00	0.00
FeO	4.71	6.89	4.15	1.32	0.95	1.02	0.00	0.09	0.13	2.08	0.20	0.93	0.26	0.47	0.47
MnO	0.08	0.17	0.08	0.00	0.00	0.03	0.01	0.00	0.00	0.16	0.08	0.08	0.00	0.00	0.00
MgO	3.91	4.70	3.72	1.03	0.99	0.87	0.00	0.07	0.06	1.38	0.07	0.57	0.17	0.56	0.46
CaO	3.49	3.32	3.53	0.72	1.25	1.40	1.95	0.62	0.65	0.56	1.12	0.96	1.45	1.63	1.55
Na_2O	7.22	5.62	6.92	8.98	9.48	9.39	12.51	12.84	13.55	8.84	9.15	9.23	10.09	9.45	9.48
K_2O	0.35	0.27	0.38	0.30	0.24	0.33	0.06	0.12	0.21	1.27	1.57	1.28	1.35	1.57	1.45
Total	99.19	99.59	99.74	99.89	99.88	99.95	99.99	99.55	99.52	100.18	99.85	99.67	99.38	99.65	99.54
Number of cations based on 6 oxygens															
Si	1.964	2.008	1.991	2.035	2.016	2.034	2.010	2.021	2.030	2.009	2.034	2.032	2.197	2.197	2.191
Ti	0.009	0.009	0.010	0.002	0.000	0.001	0.000	0.000	0.000	0.004	0.002	0.002	0.000	0.003	0.000
Al	0.891	0.800	0.881	1.012	1.025	0.999	1.000	1.006	0.975	1.006	1.032	1.010	0.789	0.776	0.793
Cr	0.000	0.004	0.000	0.000	0.001	0.000	0.002	0.000	0.000	0.000	0.000	0.000	0.000	0.000	0.000
Fe^{3+}	0.000	0.000	0.000	0.000	0.000	0.000	0.000	0.000	0.000	0.000	0.000	0.000	0.000	0.000	0.000
Fe^{2+}	0.136	0.198	0.118	0.037	0.026	0.028	0.000	0.002	0.004	0.058	0.006	0.026	0.007	0.013	0.013
Mn	0.002	0.005	0.002	0.000	0.000	0.001	0.000	0.000	0.000	0.004	0.002	0.002	0.000	0.000	0.000
Mg	0.200	0.241	0.189	0.051	0.049	0.043	0.000	0.000	0.003	0.069	0.003	0.028	0.009	0.028	0.023
Ca	0.129	0.122	0.129	0.025	0.045	0.050	0.070	0.011	0.023	0.020	0.040	0.033	0.052	0.058	0.055
Na	0.482	0.374	0.456	0.576	0.610	0.604	0.812	0.907	0.884	0.572	0.589	0.597	0.652	0.609	0.611
K	0.015	0.012	0.016	0.013	0.010	0.014	0.003	0.017	0.009	0.054	0.067	0.053	0.057	0.066	0.062
Total	3.828	3.773	3.792	3.751	3.782	3.774	3.897	3.964	3.928	3.796	3.775	3.783	3.763	3.750	3.754

Ave (n) average of n analyses, *Omp/Jad* Omphacitic Jadeite

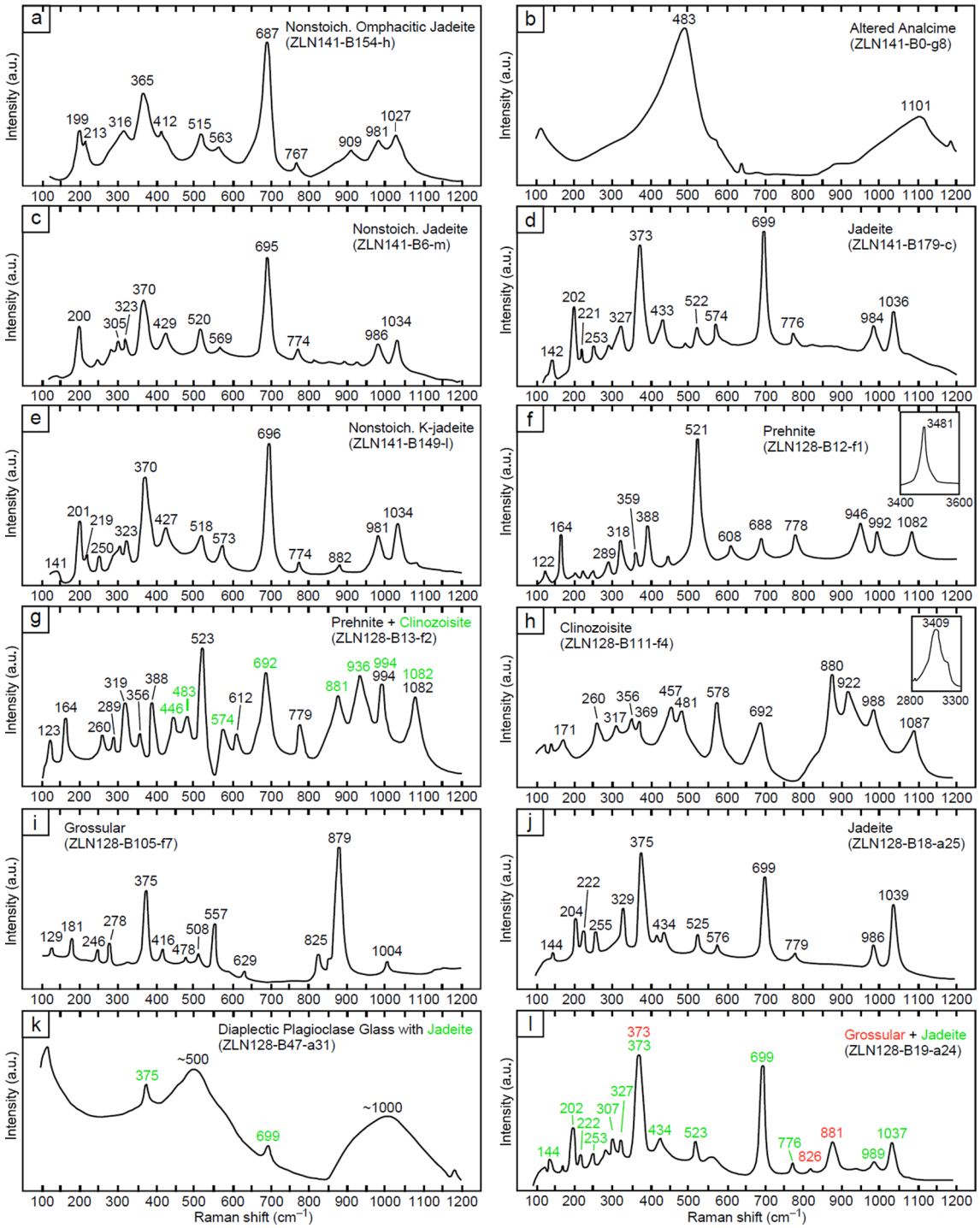

Fig. 3 Raman spectra of shock-induced minerals and glasses in samples ZLN141 and ZLN128. **a** Nonstoichiometric omphacitic jadeite within a shock vein. The relative broad form of the peaks is remarkable. **b** This spectrum clearly shows the glassy state of a former analcime veinlet. **c** Nonstoichiometric jadeite. **d** Jadeite. **e** Nonstoichiometric K-jadeite. **f** 'Pre-Ries' prehnite with indication of OH. **g** 'Pre-Ries' prehnite (black) partially replaced by clinozoisite (green). **h** Pure clinozoisite with indication of OH. **i** Grossular. **j** Spectrum of blocky jadeite. **k** Spectrum of diaplectic plagioclase glass with some jadeite. **l** Spectrum of a fine-grained grossular-jadeite assemblage at the bright ridge around DPG in Fig. 5c

stoichiometric (Table 2). Their Raman spectrum (Fig. 3d) shows two main peaks at 699 and 373 cm^{-1} as well as two peaks at 984 and 1036 cm^{-1}, typical for pure jadeite (Wang et al. 2001; Prencipe et al. 2014). It is thought that these 'huge' pyroxene grains resulted by crystallization from molten analcime material.

The volumes of DPG on the right-hand side of Fig. 2c show several linear dark zones that sometimes merge into areal zones (red arrow marks one of these numerous 'fields'). These shock-induced molten zones are Na-Si-rich and probably developed at places, where the former Ca-rich plagioclase contained cracks or fissures leading to stronger shock reverberation with fusion. Newly formed tiny crystals are indicative for presence of shock-induced melts.

On the right-hand side of the shock vein such a former sericitized Ca-rich plagioclase grain exists in close contact with the vein (Fig. 2f). This grain is completely converted to small-sized grains of nonstoichiometric K-rich jadeite with 1.2–1.6% K_2O that also show Si ≈ 2 apfu, Al ≈ 1 apfu, but a significant M2-vacancy of about 0.22 apfu (Fig. 2f; Table 2). The Raman spectrum of this phase is given in Fig. 3e. The hollow dark interstices in between these pyroxene grains could be explained by a former SiO_2-rich glass that was later dissolved.

Ca-rich high-pressure phases resulting from shock fusion of prehnite

A small contact zone of a SMV in ZLN128 with a prehnite veinlet is shown in Fig. 4a. The 200 to 600 -hick veinlet is cut by a diagonal SMV. In the contact zone of the SMV and the prehnite veinlet lots of fine-grained grossular-rich garnet are visible. In this area, the chemical composition of the 'normal' SMV (mixtures between hornblende and plagioclase compositions) was obviously influenced by additional material from the Ca-rich prehnite veinlet and this change in bulk melt composition must be the reason for the dominance of grossular (Fig. 4a). A bit further away within the SMV, magnesio-hornblende is majoritized (MajMhb) and the accompanying garnets are majoritic. At places, the SMV contains precipitates of kyanite and longish crystals of slightly nonstoichiometric omphacitic jadeite within a Ca-rich melt glass with bubbles (Fig. 4b).

At an outside distance of ~ 300 µm from the SMV, tiny crystals of clinozoisite (Clz) are beginning to grow within the original prehnite veinlet (Fig. 4c). The Raman spectra of the prehnite veinlet and the area with novel crystallizations of clinozoisite are shown in Fig. 3f, g. A sector closer to the shock vein margin shows total transformation of prehnite to clinozoisite as confirmed with the Raman spectrum in Fig. 3h. In closer proximity to the SMV, prehnite was transformed to fine-grained grossular and a darker gray-colored glassy phase. Many roundish black holes often aligned with each other are indicative for a loss of fluid after and during solidification. This fluid was derived from prehnite and, thus, was H_2O-rich (Fig. 4d).

The frequent occurrence of grossular garnet grains in ZLN128 is linked to Ca-rich prehnite material close to or within shock veins. Attempts to analyze grossular grains generally were not successful, although Raman spectra confirm the sole presence of grossular garnet (Fig. 3i). The Si and Al contents in our 'grossular' analyses are generally too high, whereas those of Ca are too low, far away from stoichiometry (Table 3). Many of these grossular grains contain small (< 1 µm) dark-gray inclusions (Fig. 4b), the character of which could not be determined. A similar observation was made by Liu et al. (2012) in an experimental study, where synthesized grossular garnet grains were found to be generally richer in Si and Al, but poorer in Ca than the ideal formula. In many cases, larger grains of grossular are poikilitic (Fig. 4e), but smaller grains seem to be homogeneous (Fig. 4f). In both cases, the Raman spectra indicate the sole phase of grossular (Fig. 3i). It is, therefore, supposed that the small roundish inclusions should be a glassy phase, but their true nature remains unknown.

Breakdown of plagioclase in a Na-Ca-rich system

Tiny crystals of 'jadeite' in DPG domains were first reported from shocked amphibolite of the Ries crater long times ago (James 1969). The break-down of analcime into blocky laths of jadeite within and in proximity to SMVs occurs in section ZLN128a (Fig. 5a). Moreover, in ZLN128 an instructive example of shock-induced transformation of DPG into jadeite and grossular is seen in Fig. 5b, c. Dark-colored interstices in the agglomerated Na-rich pyroxenes are ubiquitous. Such material may have been dissolved by a fluid-rich phase. Small-sized bright-colored clusters of grossular occur within the assembly of jadeite grains as shown in Fig. 5b–d. The Raman spectra of the newly formed grossular and jadeite are depicted in Fig. 3i, j.

The plagioclase grain was partially transformed to DPG (Fig. 5b, c; Table 1) and the Raman spectrum shows the typical undifferentiated broad 'glass-like' peak of DPG at ~ 500 cm^{-1} (Fig. 3k). The small seam at the border zone next to jadeite grains consists of a fine-grained intergrowth of jadeite and grossular (Fig. 5c and 3l). This seam was originally fused, whereas the residual DPG was shock-transformed in the solid state (von Engelhardt et al. 1967; Jaret et al. 2015).

Shock-induced phases from K-Na-rich melts produced from sericitized plagioclase

Plagioclase grains in samples ZLN128/128a and ZLN141 contain masses of irregularly distributed secondary sericite

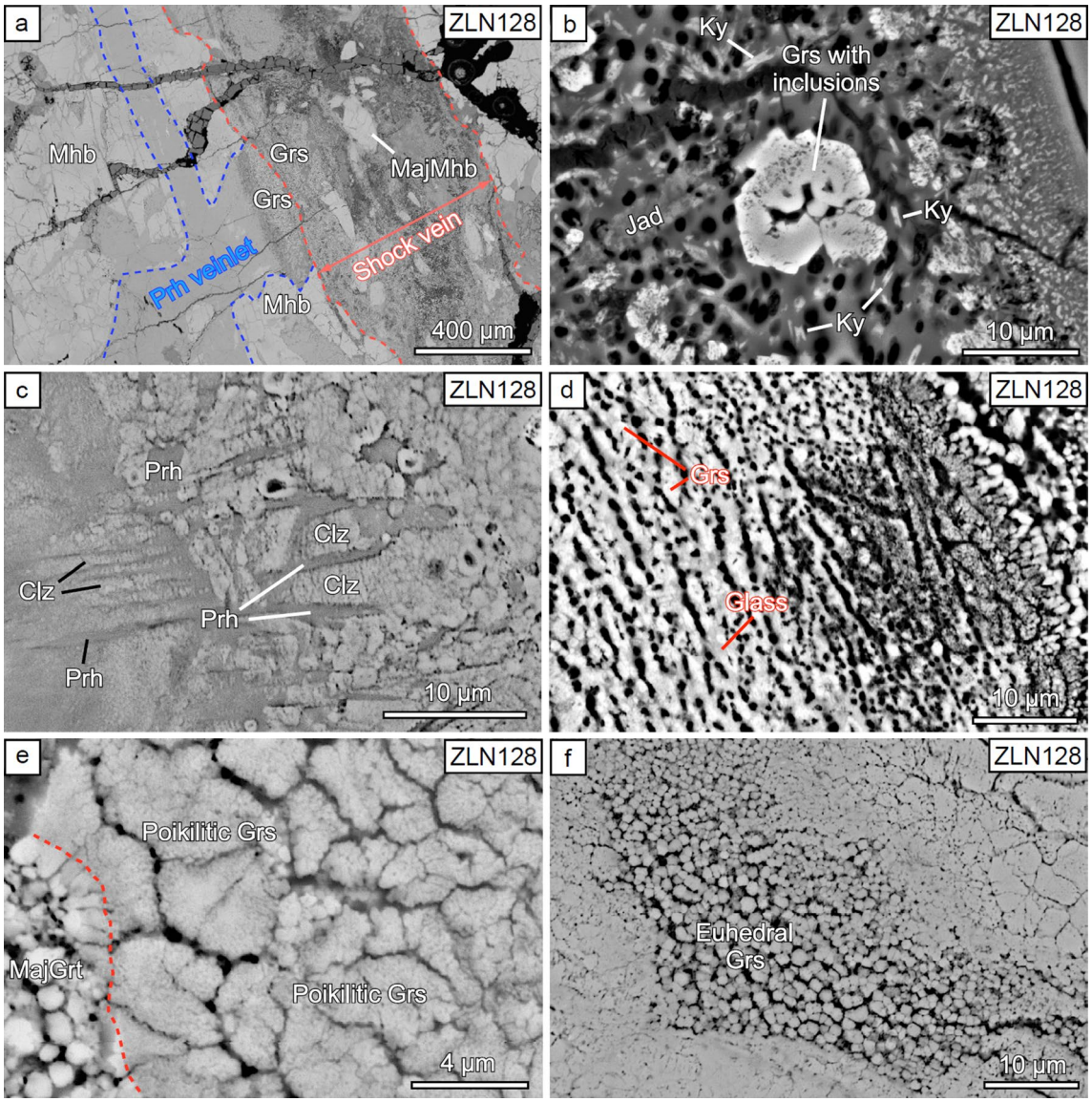

Fig. 4 BSE-images of shock-induced phases at the contact of a prehnite veinlet with a shock vein in ZLN128. **a** Contact of a prehnite veinlet (blue) with a ~ 600 µm-wide shock vein (red). The shock vein at this place is full of grossular due to admixture of prehnite melt. **b** A larger grain of grossular within a shock vein containing many dark 'glassy' inclusions. The grain is surrounded by jadeite (Jad), kyanite (Ky) and glassy material. The dark round blebs (outside grossular) suggest the presence of H_2O. **c** Initiation of clinozoisite crystallizations in the prehnite veinlet in close neighborhood to the shock vein (~ 300 µm). **d** Intimately aggregated grossular garnet grains (light) and glass (gray) directly at the edge of a shock vein (right upper corner). Note the roundish black holes that often follow each other like pearls on a chain. These hollows are probably derived from exsolved H_2O. **e** Close-up of assembled single grains of grossular. Note the poikilitic texture of individual grains. **f** Assemblage of shock-induced euhedral grossular crystals

(Fig. 1c). The sericitization is strongest in formerly Ca-rich portions of plagioclase, indicating that Ca was lost from the local system while K was gained during this process. The resultant two-phase mineral mixture of relatively Na-rich plagioclase and sericite is thermally unstable not only within, but also in the vicinity of SMVs. A first instructive example is seen in ZLN128 (Fig. 6a), where a curved end of a former sericitized plagioclase grain extends into a ~ 400 µm-thick shock vein (red arrow). Close to the vein, the grain of sericitized plagioclase was totally melted and various fine-grained high-pressure phases crystallized from the melt. The chemical compositions of these phases reflect the composition of the liquid. Some newly formed majoritic garnet grains within the former Na–K rich melt document the momentarily prevailing high pressures of the dynamic shock event (Fig. 6b, c). The chemical composition of the melt glass shows an alkali-silica-rich mode (Table 1), and the correspondent Raman spectrum is consistent with its

Table 3 Electron microprobe analyses (EMPA) and energy-dispersive X-ray analyses (EDXA) of grossular and majoritic garnet grains

Mineral	Grs	Grs	MajGrt1	MajGrt1	MajGrt2	MajGrt3	MajGrt4	MajGrt4	MajGrt4	MajGrt4	MajGrt5	MajGrt5	MajGrt5	MajGrt5
Method	EMPA	EMPA	EMPA	EMPA	EMPA	EDXA	EMPA	EMPA	EMPA	EMPA	EDXA	EDXA	EDXA	EDXA
Analysis#	128–20	128–07	128–23	128–24	128a-30	128a-49	128–67	128–69	128–74	128–75	128a-15	128a-20	128a-13	128a-124
SiO_2	42.01	41.02	47.47	47.37	46.27	47.33	45.50	46.70	46.27	47.09	42.17	41.82	42.23	42.68
TiO_2	0.06	0.03	0.54	0.32	0.78	0.29	0.00	0.00	0.03	0.00	0.12	0.00	0.00	0.00
Al_2O_3	24.22	24.19	12.98	14.36	13.81	16.94	20.53	20.54	20.18	18.95	22.32	21.92	22.17	22.35
Cr_2O_3	0.00	0.00	0.04	0.01	0.06	0.00	0.09	0.01	0.00	0.01	0.00	0.00	0.00	0.00
Fe_2O_3	0.00	0.00	0.00	0.00	0.00	0.00	0.00	0.00	0.00	0.00	0.00	0.00	0.00	0.00
FeO_{tot}	2.03	0.28	12.60	11.14	11.94	8.54	10.34	9.17	9.49	9.81	14.48	15.18	13.36	13.86
MnO	0.05	0.01	0.21	0.31	0.28	0.15	0.39	0.34	0.30	0.31	0.36	0.46	0.51	0.39
MgO	0.27	0.19	12.96	13.48	12.89	18.39	21.60	22.30	22.73	21.03	15.46	15.88	15.88	15.49
CaO	28.80	29.80	11.57	11.58	12.74	7.76	0.27	0.27	0.85	1.13	4.00	4.55	4.49	5.09
Na_2O	0.31	0.51	1.44	1.17	0.82	0.43	0.47	0.41	0.70	1.34	0.24	0.12	0.15	0.00
K_2O	0.06	0.14	0.14	0.10	0.16	0.14	0.91	0.70	0.12	0.20	0.29	0.12	0.14	0.15
Total	97.81	96.17	99.95	99.84	99.75	99.97	100.10	100.44	100.67	99.87	99.44	100.05	99.93	99.95
Number of cations per formula unit based on FeO_{tot} = FeO and 12 oxygen anions:														
Si	3.145	3.118	3.502	3.469	3.424	3.370	3.214	3.256	3.228	3.320	3.083	3.056	3.075	3.098
Ti	0.004	0.002	0.030	0.018	0.044	0.015	0.000	0.000	0.002	0.000	0.007	0.000	0.000	0.000
Al	2.138	2.167	1.129	1.239	1.204	1.422	1.709	1.688	1.659	1.576	1.923	1.888	1.902	1.911
Cr	0.000	0.000	0.002	0.000	0.003	0.000	0.005	0.001	0.000	0.001	0.000	0.000	0.000	0.000
Fe^{3+}	0.000	0.000	0.000	0.000	0.000	0.000	0.000	0.000	0.000	0.000	0.000	0.000	0.000	0.000
Fe^{2+}	0.127	0.018	0.777	0.682	0.739	0.508	0.611	0.535	0.554	0.579	0.886	0.928	0.874	0.841
Mn	0.003	0.000	0.013	0.019	0.017	0.009	0.023	0.020	0.018	0.019	0.022	0.028	0.032	0.024
Mg	0.030	0.022	1.426	1.471	1.422	1.952	2.275	2.321	2.364	2.212	1.685	1.729	1.723	1.669
Ca	2.310	2.426	0.914	0.908	1.010	0.592	0.020	0.020	0.064	0.085	0.313	0.357	0.350	0.396
Na	0.045	0.076	0.206	0.166	0.118	0.059	0.064	0.056	0.094	0.184	0.035	0.017	0.022	0.000
K	0.006	0.014	0.013	0.009	0.015	0.013	0.082	0.062	0.010	0.018	0.027	0.011	0.013	0.014
Total	7.808	7.843	8.012	7.981	7.996	7.940	8.003	7.959	7.993	7.994	7.981	8.014	7.991	7.953
P (GPa)[a]	–	–	17.43	16.71	16.25	13.29	8.92	9.35	9.51	11.39	8.46	8.19	8.43	8.74

[a]Pressure values for majoritic garnet grains were calculated with the barometer for metabasites from Wijbrans et al. (2016)

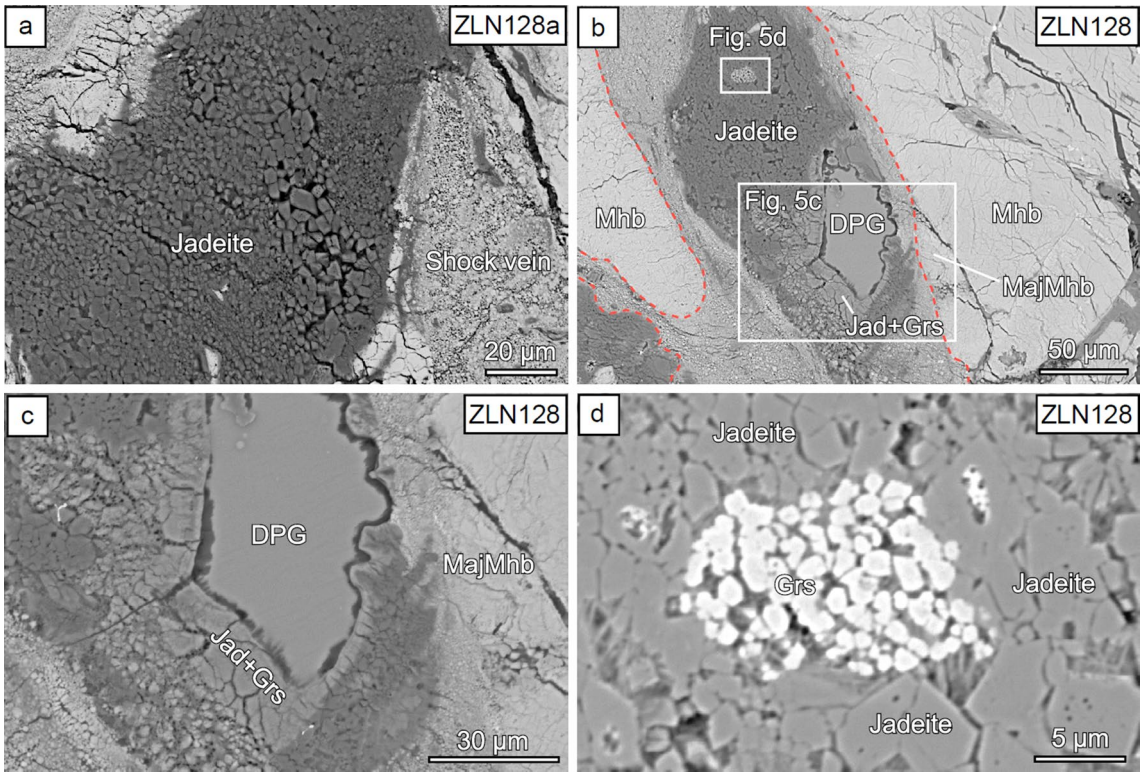

Fig. 5 Occurrence of normal jadeite within ZLN128a/ZLN128. **a** Assemblage of blocky jadeite grains close to a shock vein. **b** BSE image of a former plagioclase grain enclosed within a shock vein. The upper part consists of jadeite and patches of grainy grossular, while the lower part contains relic DPG. Shock-induced grains of jadeite and grossular in plagioclase of the host. **c** Close-up of lower part of Fig. 5b with a relic grain of diaplectic plagioclase glass (DPG) surrounded by a rim of jadeite + grossular. **d** Close-up of an assemblage of grossular (bright grains) within aggregated jadeite grains

glassy state (Fig. 7a). Within this melt glass very small grains of kokchetavite are assembled (Figs. 6b and 7b).

The K-feldspar polymorph kokchetavite was explicitly identified by its characteristic triple of Raman bands at ~ 106 cm^{-1}, 388 cm^{-1} and 833 cm^{-1} (Fig. 7b). The positions of the first two bands are clearly different from those of K-cymrite at ~ 115 cm^{-1} and 381 cm^{-1} (Kanzaki et al. 2012; Mikhno et al. 2013; Ferrero et al. 2016; Romanenko et al. 2021). In our sample ZLN128/128a nanometer-sized grains of kokchetavite are often surrounded with albitic jadeite (Fig. 6c) as is also indicated by Raman spectra (Fig. 7c). Moreover, another relatively strong peak at ~ 760 cm^{-1} exists in most of our Raman spectra of coexisting jadeite and kokchetavite (Fig. 7c). This striking, relatively broad peak is completely lacking in the Raman spectra of both single phases (Fig. 7b, p). Furthermore, the local bulk chemistry of the system (K-Na-rich; Table 1) and the spectral position of this peak give strong evidence for the presence of liebermannite (Lib) with its diagnostic major peak at 760–765 cm^{-1} (e.g. Liu et al. 2009; Ma et al. 2018; Chen et al. 2019). We were not able to identify Lib in several BSE images of ZLN128, probably due to the generally very small grain size in the nm-scale. Nevertheless, in nine Raman analyses of these kokchetavite-bearing jadeite grains, we found this peak at ~ 760 cm^{-1}, and only in four analyses this peak did not occur. Such tiny aggregations of Lib were also illustrated by Langenhorst and Poirier (2000b) and Sharp and DeCarli (2006).

In our sample ZLN128, the Na-rich high-pressure phase in the alkali-rich melt glass is albitic jadeite (Figs. 6c, d, 7d) as defined by Ma et al. (2022). Our attempts to analyze this clinopyroxene resulted in analyses that have Si ≈ 2.19 apfu, Al ≈ 0.8 apfu and a strong M2-vacancy of ~ 0.25 apfu (Table 2). Kokchetavite and albitic jadeite are accompanied by a few grains of xenoblastic majoritic garnet with strong reflectivity (Fig. 6c, d). The chemical composition of the garnet phase records the current crystallization pressure in the local melt (Table 3) as will be discussed later.

Irregular patches of K-rich white mica occur frequently in DPG volumes close to SMVs. Electron microprobe analyses of an original sericitic muscovite (Si ≈ 3.11 apfu) in plagioclase and a phengite (Si ≈ 3.4 apfu) formed during shock are given in Table 1. Our Raman shift spectrum of phengite is shown in Fig. 7e. Using the data presented in Fig. 7.5 of Li et al. (2011), the peak positions at 196, 264, 416, 640 and 703 cm^{-1} suggest Si contents between 3.2 and 3.3 apfu.

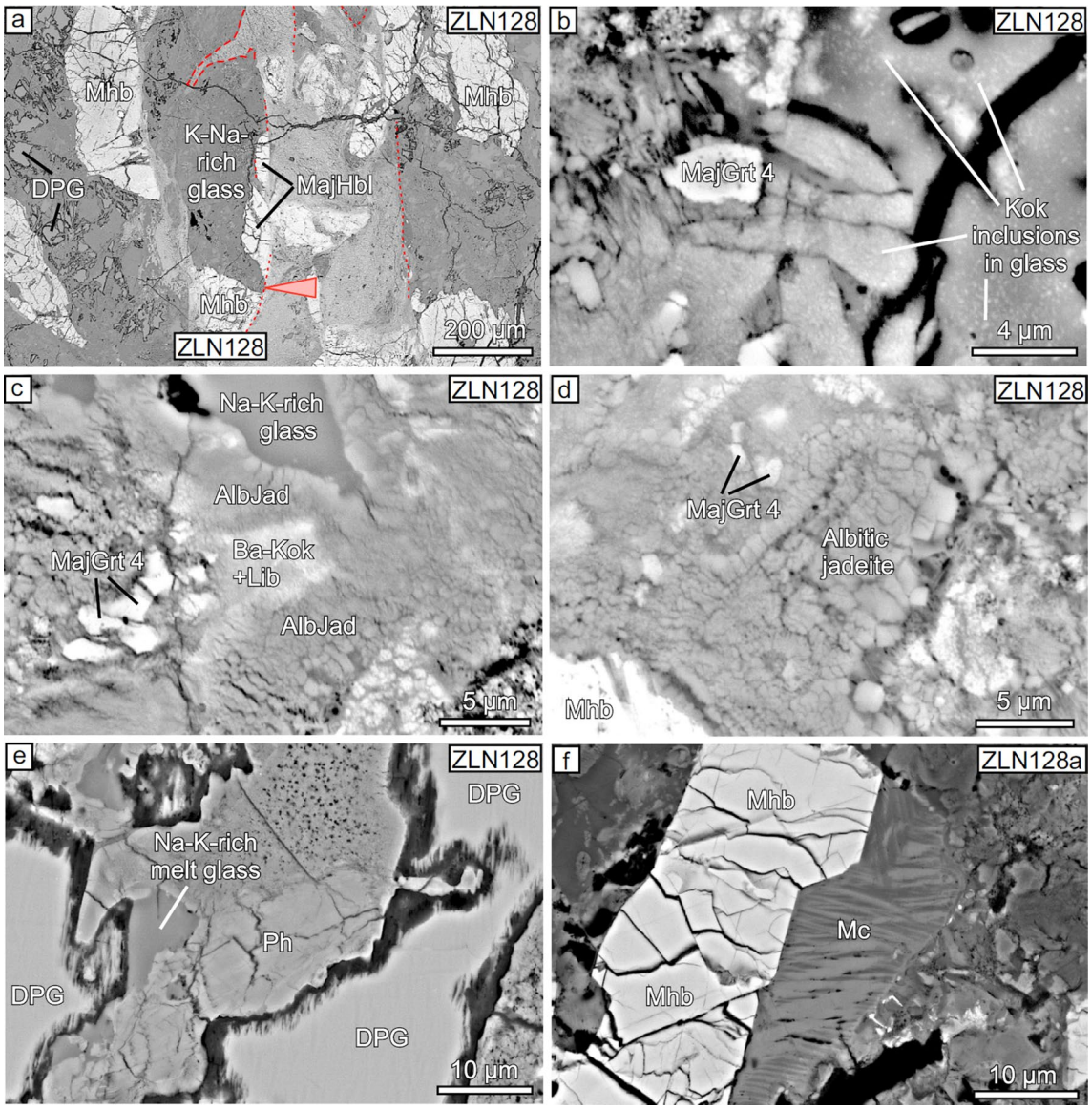

Fig. 6 Various minerals in a Na–K-rich melt glass in ZLN128/128a. **a** BSE image of a former sericitized plagioclase grain that is now converted into a Na–K-rich glass that has a tip (red arrow) into a shock vein filled with majoritic garnet 1. The SMV is marked with red dashed lines. Along the right rim of the glass exist some grains of a majoritized hornblende (MajGrt). **b** Fine-grained inclusions of nanometer-sized kokchetavite (bright spots) in a Na–K-rich melt glass. **c** Liebermannite (Lib) and Ba-rich kokchetavite (Ba-Kok) (light gray) and albitic jadeite (medium gray) together with Na–K-rich glass. Within the left part of the figure several grains of MajGrt 4 are visible **d** Majoritic garnet 4 and grayish albitic jadeite grains. **e** Grain of shock-induced phengitic muscovite (Ph) in contact with Na–K-rich glass. **f** Crossing of light and dark lamellae within a primary grain of microcline-perthite (Mc). The bright grain on the left-hand side consists of a magnesio-hornblende (Mhb) of the host amphibolite

A further example of a K-Na-rich melt glass occurs in ZLN 128a (Fig. 1c, arrow 1). Besides kokchetavite and albitic jadeite, some grains of grossular and clinozoisite may locally be present (not shown here). This seems at a first glance anomalous. However, prehnite in amphibolite ZLN128/128a appears also sporadically within some former grains of variably sericitized plagioclase. When shock-transformed, such heterogeneous mineral aggregates may be transformed to chemically heterogeneous glass with domains that are either richer in Ca or in K–Na, depending on the degree of former sericitization of plagioclase. This explains why grossular and clinozoisite are present only locally. Moreover, the alkali-rich melt glass domains of ZLN128a may rarely contain some larger grains of microcline with crossing lamellae (Fig. 6f; Table 1) that are thought to be primary.

Beyond that, we also found a former strongly sericitized plagioclase grain as clast within a SMV in ZLN141 (Fig. 1a;

red arrow 4). The wedge-shaped clast of DPG contains µm-sized crystals of liebermannite (K-hollandite) laying within irregular domains of K-Na-rich melt glass (Fig. 8a, b). The distribution of K and Ca within the small areal portion is shown in Fig. 8c, d. At two places (red points in Fig. 8b) we got Raman spectra with the strongest peaks of liebermannite at 218 cm^{-1}, 276 cm^{-1} and 759 cm^{-1} (Fig. 8e). The broad peak at ~ 500 cm^{-1} belongs to the alkali-rich melt glass that hides additional small peaks of Lib at about 521 cm^{-1} and 539 cm^{-1} (Liu et al. 2009; Chen et al. 2019).

Existence of grossular, vuagnatite, and lawsonite + coesite in Ca-rich domains

In sample ZLN128a (Fig. 1c, lower red arrow 2), the volume between a SMV (right upper corner) and a large grain of majoritized magnsio-hornblende (MajMhb) at the left (Fig. 9a) is characterized by a three-part zone of (1) grossular (Grs) grains adjacent to the SMV, (2) coexisting grossular (Grs) + vuagnatite (Vua) at larger distances of about 20–50 µm from the SMV and (3) isolated grains of majoritic garnet 5 along the contact with chlorite and/or majoritized magnesio-hornblende. In all three subzones, the minerals are surrounded by a dark-gray clayey matrix of kaolinite that most probably resulted from residual liquid transformed to glass (Fig. 9a, b). Due to the small grain size of grossular and vuagnatite, their identity could only be determined by Raman spectroscopy (Fig. 7g). These two minerals form heterogeneous patches of roundish to lobate shape (Fig. 9b) that point to rapid growth of these two phases from an originally Ca-rich silicate melt. We assume that this shock-induced liquid was derived from Ca-rich plagioclase. It is striking that vuagnatite only occurs at some distance from the hot SMV (Fig. 9a).

On the right-hand side of the SMV, a similar succession of mineral zones occurs (Fig. 9c). Grossular alone at the contact to the SMV is followed by a zone of Grs + Vua, that grades into a zone of single vuagnatite (Fig. 9d). The latter zone may then be bordered by DPG and is partly converted to a fine-grained intimate mixture of lawsonite (Lws) and coesite (Coe) (Fig. 9c, d, f). This sequence of mineral zones was documented by Raman spectroscopy (Fig. 7h–j). More remote to this *P–T* dependent sequence of high-pressure phases at a distance within ~ 320 µm, there exist primary minerals of the host amphibolite (ZLN128a). The fine-grained lawsonite + coesite assemblages are in close contact with diaplectic Ca-rich plagioclase glass (DPG) as shown in Fig. 9c, f.

Between a SMV shown in Fig. 10a (lower left) and a large grain of marginally majoritized hornblende (MajMhb), there exists a zone rich in montmorillonite assumed to represent former glass. Adjacent to MajMhb, this zone contains subhedral to longish Ca-rich majoritic garnet grains, while small isometric majoritic garnet 2 grains are present near to the contact to the SMV (Fig. 10b, c). Results of EMPA analyses of the Ca-rich majoritic garnet grains yielded compositions far away from garnet stoichiometry. However, even though most of these grains show fluorescence, their Raman shift spectra (Fig. 7k) point to a Ca-rich majoritic garnet with significant amounts of Fe and Mg (main band at 901 cm^{-1} instead of ~ 880 cm^{-1}). It is thought that the 'anomalous' chemistry of the Ca-rich majoritic garnets is due to tiny glass inclusions that cannot be clearly recognized in our BSE images.

A large grain of amphibole (Mhb) of Fig. 10a shows a marginal zone with higher reflectivity. This bright region consists of shock-induced majoritized hornblende (MajMhb). The characteristic Raman spectrum is shown in Fig. 7m. The broad shoulder at 800–900 cm^{-1} marks the specific Raman vibrancy of the majorite component (Kunz et al. 2002; Gillet et al. 2002). Intense brown–red colors in transmitted light characterize these striking shock-induced garnet-rich zones in amphiboles in touch with SMVs (Stähle et al. 2011: Fig. 2a). However, the strongest Raman band at 915 cm^{-1} (Fig. 7m) differs slightly from that of majoritic garnet (920–922 cm^{-1}) formed from liquids as shown in Fig. 7n, o.

At another place of the latter SMV, along the edge with chloritic material, there exists a small fringe of lathy crystals (Fig. 10d). We suppose that these newly formed grains are shock-induced crystals of vuagnatite (Vua) as was revealed by Raman spectroscopy (Fig. 7l). However, the main Raman bands are very broad and look rather unspecific. Moreover, the chemical analysis shows remarkable contents of MgO and FeO. It is well possible that these components are derived from interstices filled with montmorillonite (Mnt) material (Fig. 10d).

Majoritic garnet within and outside SMVs

In sample ZLN128/128a, majoritic garnet not only occurs within SMVs (Stähle et al. 2011, 2017), but also in their neighborhood, where different textural types can be distinguished. Analyses of these garnets are given in Table 3. Subsequently, we will characterize these five various types of majoritic garnet, and we will give crystallization pressures calculated according to Wijbrans et al. (2016) as follows:

(1) The first type of majoritic garnet (MajGrt 1) occurs within SMVs and its grains are mostly hypidiomorphic (Fig. 10a–c; Table 3). Chemical compositions of seven majoritic garnet grains show Si = 3.35–3.50 apfu, Na = 0.12–0.21 apfu, and Ca = 0.89–1.48 apfu, resulting in crystallization pressures between 16.3 and 18.6 GPa with a mean of 17.0 ± 0.8 GPa (1 s).

(2) Hypidiomorphic grains (MajGrt 2) also occur outside of, but close to the contact with SMVs (Fig. 10b, c).

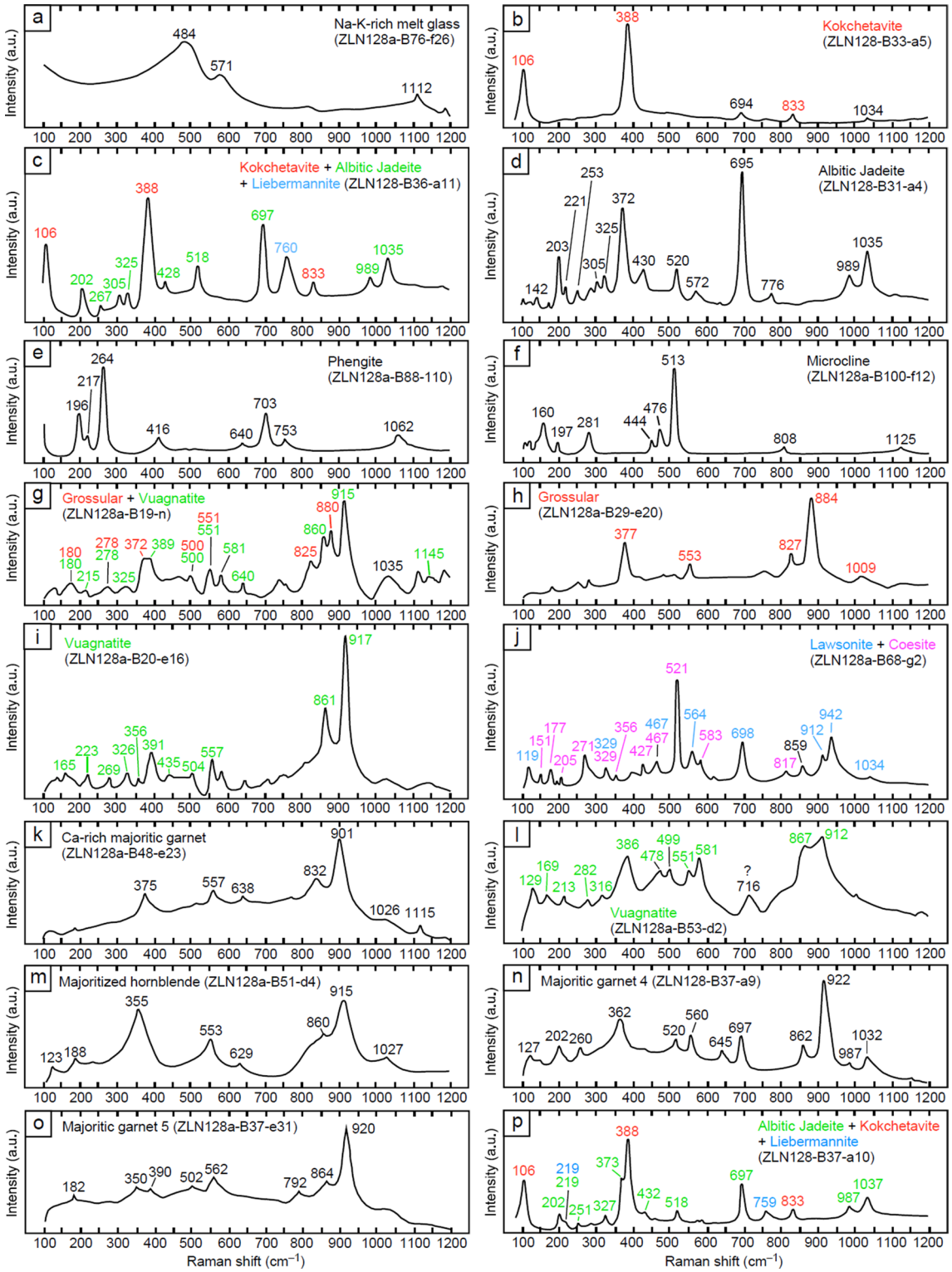

The space between individual grains consists of montmorillionite and is thought to represent former residual glass. Their compositions are Si ≈ 3.42 apfu, Na ≈ 0.12 apfu and Ca ≈ 1.01 apfu (Table 3) resulting in a pressure of 16.3 GPa.

(3) A small seam of majoritic garnet (MajGrt3) along the grain of partially majoritized magnesio-hornblende occurs at some distance to SMVs (Fig. 10b, red arrow). This garnet shows Si ≈ 3.37 apfu, Na ≈ 0.06 apfu, and Ca ≈ 0.59 apfu, resulting in a pressure of 13.3 GPa (Table 3).

◂**Fig. 7** Raman spectra of shock-induced minerals and glasses in ZLN128 and ZLN128a. **a** Alkali-rich melt glass. **b** Kokchetavite; a triple at 106 cm^{-1}, 388 cm^{-1} and 833 cm^{-1} Raman shift is characteristic. **c** Multiphase Raman spectrum of kokchetavite and albitic jadeite. Note a single band at 760 cm^{-1} Raman shift. It belongs to the strongest band of liebermannite. **d** Albitic jadeite. **e** Phengitic muscovite. **f** Microcline. **g** Composite Raman spectrum of grossular/vuagnatite. **h** Grossular. **i** Vuagnatite. **j** Composite Raman spectrum of lawsonite/coesite. **k** Ca-rich majoritic garnet. **l** Lath-shaped vuagnatite in ZLN128a. Note the broad Raman bands. **m** Shock-induced majoritic hornblende. The broad shoulder at 800–900 cm^{-1} characterizes the majoritic component. **n** Spectrum of majoritic garnet in an alkali-rich melt glass (MajGrt 4). **o** Spectrum of a majoritic garnet in a clayey matrix (MajGrt 5). **p** Raman spectrum of the assemblage kokchetavite + liebermannite + albitic jadeite in K-Na-rich melt glass close to MajGrt 4 in ZLN128. Note the single peak at 759 cm^{-1} Raman shift of liebermannite

(4) Xenoblastic majoritic garnet grains (MajGrt 4) in close association with liebermannite, kokchetavite and albitic jadeite occur within K-Na-rich melt glass (Fig. 10e). A Raman spectrum of this garnet type is given in Fig. 7n. The grains are characterized by Si = 3.21–3.32 apfu, Na = 0.06–0.18 apfu and Ca = 0.02–0.08 apfu, resulting in *P* values of 8.9–11.4 GPa (Table 3).

(5) Solitary xenomorphic grains of majoritic garnet (MajGrt 5) occur between MajHbl and/or chlorite and the zone of grossular + vuagnatite (Fig. 10f). A Raman spectrum is given in Fig. 7o. The composition of MajGrt 5 is only slightly majoritic with Si = 3.06–3.10 apfu, Na = 0.00–0.04 and Ca = 0.31–0.40 apfu, resulting in pressure values of 8.2–8.7 GPa (Table 3).

Discussion

Behavior of water during shock metamorphism

Input of water generally lowers the fusion points and enhances diffusion rates of the ionic constituents in melts for nucleation and growth of new mineral phases. In marked contrast to most shocked meteorites that are nearly dry, coarse-grained terrestrial target rocks may still contain primary ('pre-shock') OH-bearing minerals adjacent to or even within shock veins, despite high shock-metamorphic temperatures. Before the Ries impact, the Variscan amphibolitic rocks in the basement contained many OH-bearing minerals, such as primary magnesio-hornblende and secondary chlorite, sericite, prehnite, and analcime. If a shock vein traverses a pre-existing veinlet with analcime or prehnite or an originally Ca-rich domain of a larger plagioclase grain that is sericitized, melting may occur not only within the shock vein, but also in its neighborhood in which OH-bearing minerals are present. Moreover, the examples for such a situation as presented in this paper show that even shock-induced high-*P* mineral phases such as lawsonite, clinozoisite and vuagnatite may still contain water that originally was present in pre-shock minerals. This water not only lowers the solidus of MORB, but also enhances the transport of ions and metamorphic reactions rates.

Formation of liebermannite

Recently Ma et al. (2018) characterized liebermannite from the Martian meteorite Zagami. This mineral is a high-pressure modification of K-feldspar and was first synthesized by Ringwood et al. (1967). These authors underlined the enormous change in density of this phase from 2.55 to 3.84 g cm^{-3}, an increase of ~ 50%. The formation of the 1–5 µm large liebermannite crystals in ZLN141 (Fig. 8a, b) was favored by their occurrence within a clast of DPG, which was enclosed in the matrix of a SMV. The surrounding majoritic garnets indicate high crystallization pressures of ~ 17 GPa (Stähle et al. 2017). The sixfold coordinated dense potassium-bearing phase liebermannite was first identified in the Ries crater and, to the best of our knowledge in the assemblages of terrestrial rocks as well.

Formation of albitic jadeite together with liebermannite and kokchetavite in Na–K-rich melt glass

Tiny grains of albitic jadeite with Si = 2.19 apfu and a M2-deficit of ~ 0.25 were detected within local melt glass domains (Fig. 6c, d; Table 2). An aggregate of similar albitic jadeite grains surrounded by majoritic garnet grains was found by Ma et al. (2020, 2022) within a SMV of another amphibolite from the Ries (ZLN100) that originally was described by Stähle et al. (2011, 2017). From the composition of majoritic garnet nearby albitic jadeite in this sample, Ma et al. (2022) postulated formation pressures of 18–22 GPa using the calibration method of Collerson et al. (2010). However, using the barometer equation of Wijbrans et al. (2016) yields a lower pressure of 17.8 GPa.

The low-*P* boundary of the stabiltiy field of Lib is at pressure values of ~ 9.0 GPa at 600 °C and ~ 10.3 GPa at 1700 °C (Urakawa et al. 1994; Nishiyama et al. 2005). At lower pressure values, Lib has been shown to be replaced by Si-wadeite + kyanite + coesite as follows:

$$2\,KAlSi_3O_8 = K_2Si_4O_9 + Al_2SiO_5 + SiO_2$$

(Yagi et al. 1994; Urakawa et al. 1994; Yong et al. 2006). Formation pressures of the Lib-bearing assemblage can be estimated from chemical analyses of MajGrt 4 grains that coexists with Lib, albitic jadeite, and kokchetavite (Table 3) within an area of about 7 × 7 μm^2 (Fig. 10e).

Kokchetavite (Kok) together with K-cymrite ($KAlSi_3O_8 \cdot nH_2O$; $0 < n \leq 1$) was first discovered as

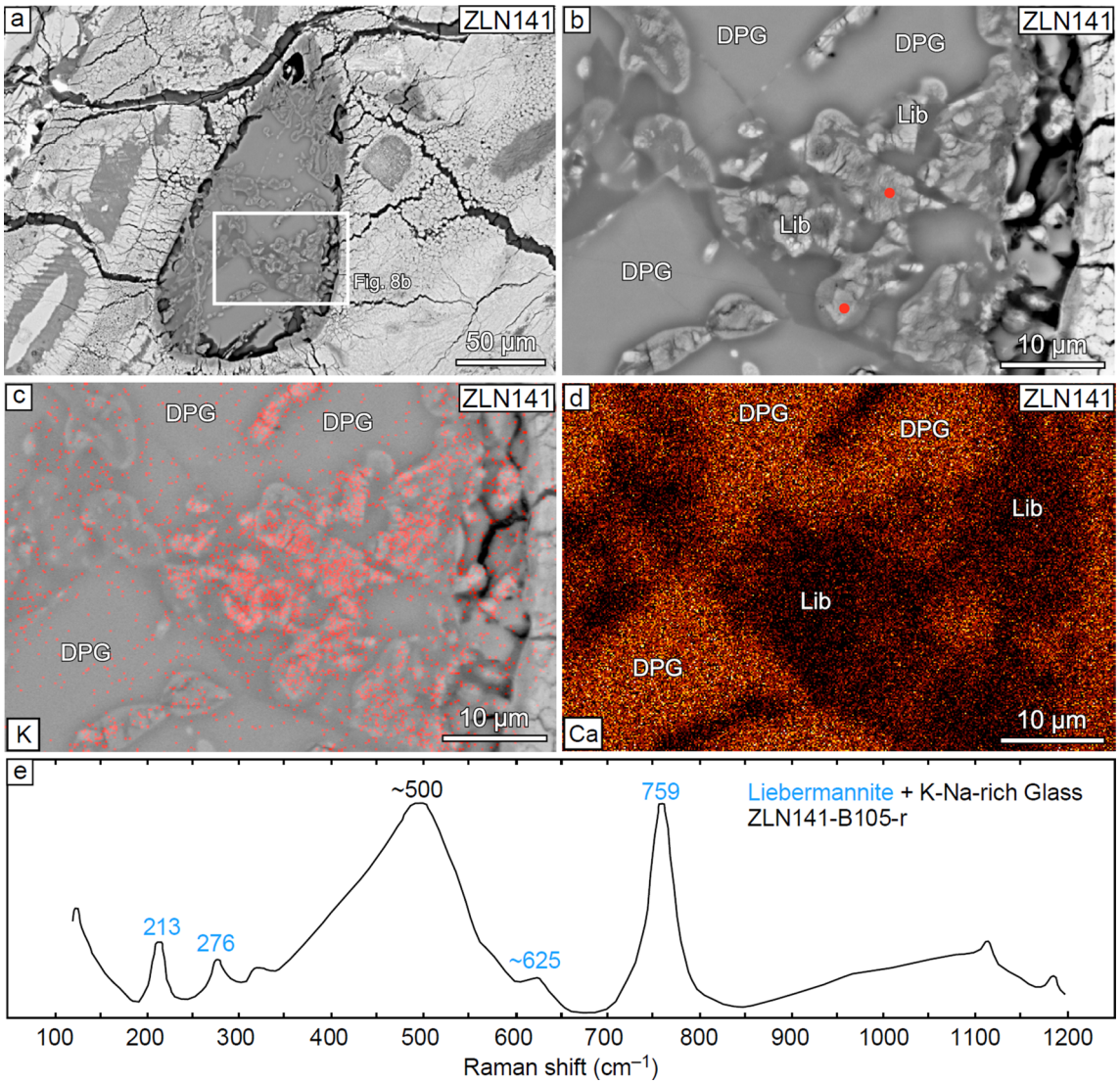

Fig. 8 Genesis of liebermannite within a former sericitized plagioclase grain in ZLN141. **a** A former sericitized plagioclase grain now consists of diaplectic plagioclase glass (DPG) and areas of liebermannite (Lib) that were generated in sericitized portions of the former plagioclase. The grain occurs as clast within SMV. **b** Details of a. Note the red points where the Raman spectra of liebermannite came from. **c** K distribution in the area of b. **d** Ca distribution in the area of b. **e** Raman spectrum of a liebermannite-rich portion and a mixed glass of sericite and DPG

µm-sized inclusions in clinopyroxene and garnet in the Kokchetav ultrahigh-pressure complex (Hwang et al. 2004). It was erroneously assumed that both phases are characterized by the same space group (P6/mmm) and that Kok is only formed by continuous dehydration of K-cymrite (Mikhno et al. 2013; Ferrero et al. 2016). Moreover, Romanenko et al. (2021) experimentally produced K-cymrite and dehydrated this phase to Kok. These authors also found that the space group of Kok is P6/mcc and not P6/mmm as assumed before. Therefore, the reaction K-cymrite = kokchetavite + H_2O cannot any longer be regarded as a second-order reaction and Kok does not necessarily seem to be a metastable phase. We should, however, not forget that this mineral is a low-density phase (~ 2.45 g cm^{-3}) and was observed to be stable at < 3 GPa in high-pressure granulites of the Bohemian Massif (Ferrero et al. 2016).

In the shocked Ries amphibolites, Kok occurs within K-Na-rich melt glass that was produced by low-*T* melting of a sericitized Na-rich plagioclase. We did not find K-cymrite. Instead, Kok occurs in intimate association with Lib and albitic jadeite (Figs. 6c, 10e). So far, we could not observe the exact textural relationship between liebermannite and kokchetavite, but it could well be that Kok was retrogressively formed from liebermannite or crystallized late as a single phase on pressure release.

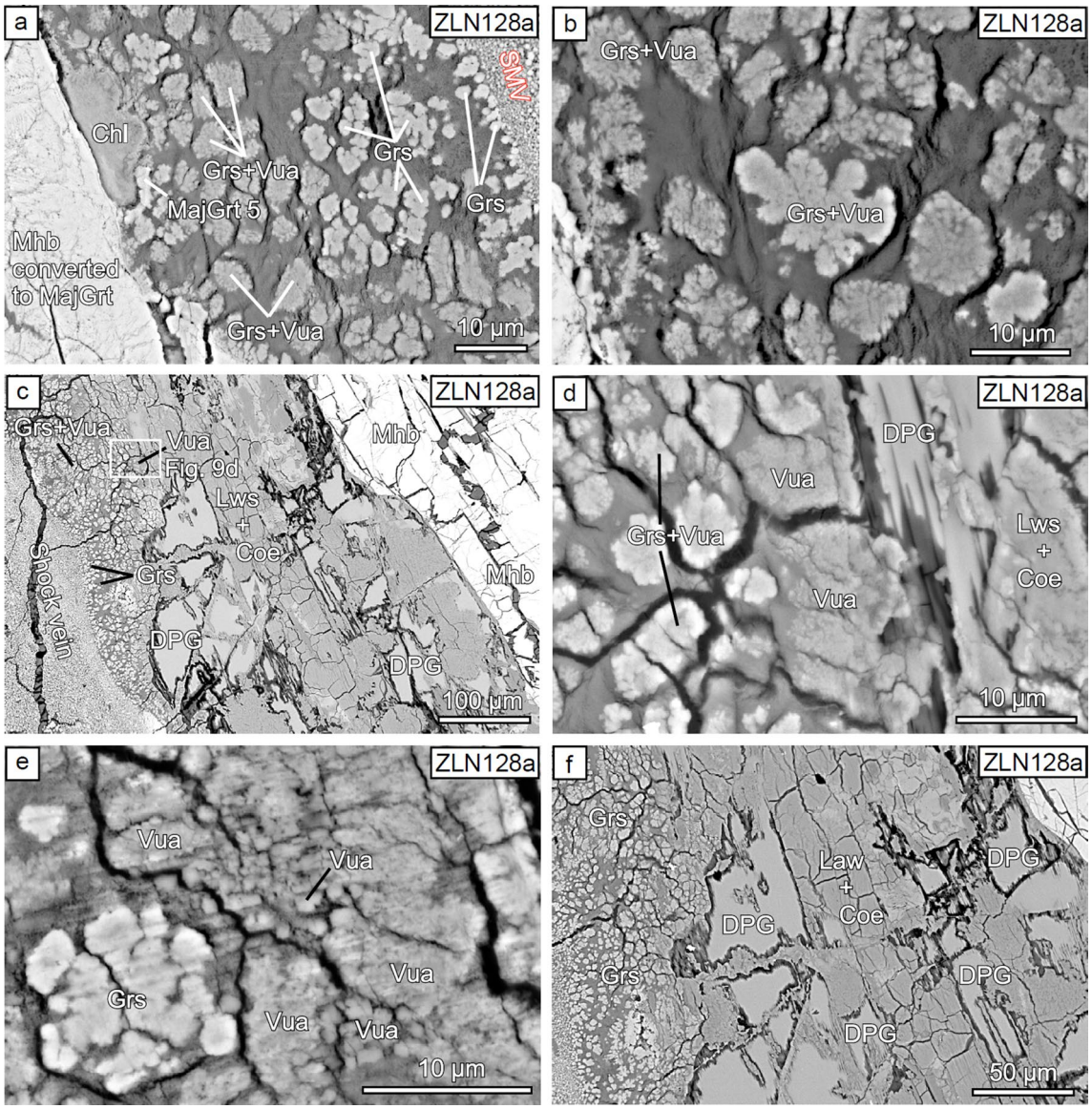

Fig. 9 Shock-induced assemblages of vuagnatite/grossular and lawsonite + coesite in ZLN128a. **a** This BSE-picture shows a zone in between a SMV (on the upper right) and a larger primary grain of magnesio-hornblende (Mhb) on the left. The rim of this Mhb grain is shock-converted to majoritic garnet. Note the chlorite grain adjacent to MajHbl. This grain is partially surrounded by MajGrt 5. The interspace between MajHbl and the SMV is characterized by a clayey matrix (medium gray) that represents former glass. Fine grained aggregates of grossular (near to the SMV) and intergrown patches of grossular + vuagnatite near to the magnesio-hornblende. **b** Close-up of rounded to lobate patches of intergrown grossular + vuagnatite in a clayey matrix. Originally these intergrowths formed in a Ca-rich high-pressure melt. After their crystallization, the remaining melt altered to a clayey matrix rich in kaolinite (at post-shock times). **c** Heterogeneously composed zone between a shock vein (left) and a magnesio-hornblende grain (right). The light gray patches in the central part consist of diaplectic plagiclase glass (DPG). Note the zones of grossular and grossular + vuagnatite close the shock vein. The occurrence of a sole vuagnatite is indicated. Note the NNE-SSW oriented strip of lawsonite + coesite in the center of the picture. **d** Detail of Fig. 9c: Fine-grained monomineralic assemblage of vuagnatite (center of the picture). The light patches on the left are intergrowths of grossular + vuagnatite. On the right-hand site there is DPG and a zone of lawsonite + coesite. **e** Single grains of vuagnatite are shown in the center. The light-colored grains at the bottom left are aggregations of grossular grains. **f** Detail of the center of Fig. 9c: A ~ 50 µm-wide band of fine-grained lawsonite + coesite is displayed in the center. On both sides and inside of this lawsonite + coesite (Lws + Coe) assemblage are relic portions of DPG. On the left side, there is a zone beside the shock vein consisting of grossular grains within a clayey matrix interpreted as former melt

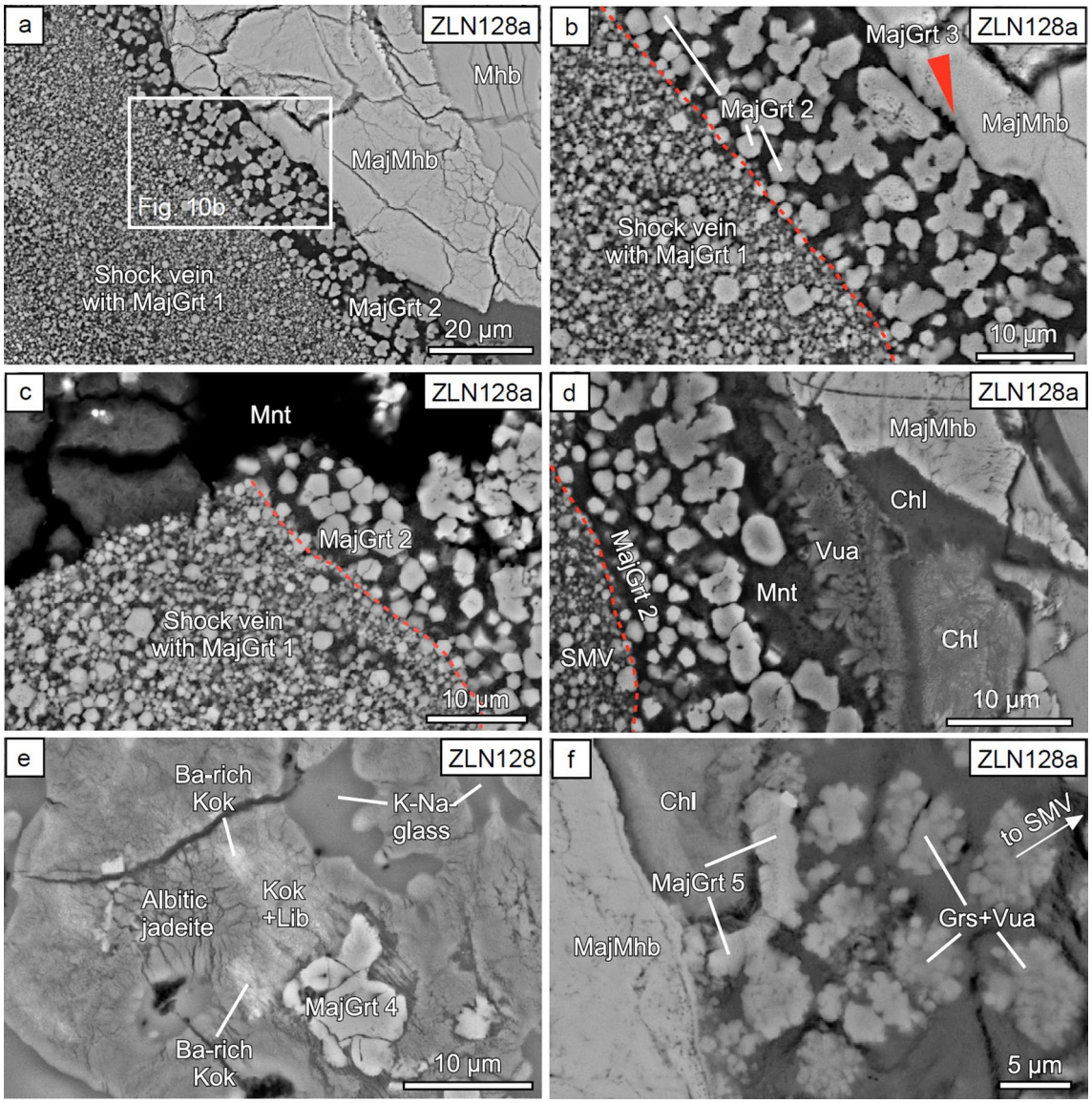

Fig. 10 Occurrence of majoritic garnet in ZLN128/128a. **a** Between a shock vein with a multitude of majoritic garnet 1 grains (MajGrt 1) and a large grain of relict magnesio-hornblende (Mhb) that is strongly majoritized (MajMhb), there is a zone of MajGrt 2 grains at the edge along SMV. In front of the magnesio-hornblende occur Ca-rich majoritic garnets. **b** Close-up of Fig. 10a: Surrounding of a shock vein (lower left) is formed by a zone of MajGrt 2 grains that are 'embedded' in montmorillonite (Mnt) grown from former glass (residual melt after crystallization of MajGrt 2). Note the small seam of MajGrt 3 (red arrow) along the edge of MajMhb. **c** Shock vein with smaller majoritic garnet 1 grains is followed by an adjacent zone of larger MajGrt 2 grains that also crystallized from a melt (now recrystallized to Mnt). **d** At further distance from the shock vein, a ~ 5 µm-wide zone of lathy vuagnatite (Vua) is visible followed by majoritized magnesio-hornblende (MajMhb) and chlorite (Chl). **e** At the left-hand side of a larger bright grain of majoritic garnet (MajGrt 4), a zone of very fine-grained kokchetavite (Kok) and lieberman-nite (Lib) occurs. The brighter parts of this zone are caused by local enrichments of Ba (Ba-rich Kok). Grains of albitic jadeite occur on the left. The original Na–K-rich melt glass is seen in the upper right-hand part of the picture. **f** A curved row of majoritic garnet grains (MajGrt 5) embedded in kaolinite are shown in the center of the photograph. There are also grains of chlorite (Chl) at the margin of MajMhb. On the right-hand side there are patches of intergrown gros-sular + vuagnatite (Grs + Vua)

It will be necessary to investigate this very fine-grained association of the three phases by means of a transmission electron microscope.

Formation of vuagnatite

The detection of vuagnatite within the shocked amphibo-lite ZLN128a was only possible by the usage of Raman spectroscopy. Vuagnatite in nature was early observed in

low-grade high-*P*/*T* metamorphic rocks of the Franciscan formation in California (Pabst 1977) and in metasomatic rodingitic dykes of the Turkish Taurus Mountains (Mc Near et al. 1976; Sarp et al. 1976). Moreover, it occurs in veins cutting serpentinite rocks from New Zealand (Craw et al. 1979) and from Shima Peninsula in Japan (Matsubara et al. 1977). This mineral is so far considered to have formed under metamorphic conditions of the prehnite-pumpellyite facies, if P_{H2O} is high enough (Pabst 1977). Despite the observed exclusive occurrence of vuagnatite in natural low-grade rocks, Pabst (1977) predicted that this mineral must be a high-pressure phase due to its calculated high density of 3.416 g/cm^3. Interestingly, vuagnatite was never experimentally synthesized in the chemical system CaO-Al_2O_3-SiO_2-H_2O (CASH), even at elevated pressures (Schmidt 1995; Ono 1998; Poli and Schmidt 2002). Vuagnatite in shocked Ries rocks (ZLN128a) is derived from Ca-rich plagioclase ($An_{71–75}$) and was coprecipitated preferentially with grossular (Fig. 9a–e). It is striking that grains of grossular that occur close to SMVs constantly lack a coprecipitation of vuagnatite as may be seen in Fig. 9a, c.

P–T estimates based on majoritic garnets and lawsonite in melt pools outside SMVs

The chemical composition of majoritic garnets 4 and 5 (Fig. 10e, f) record effectively the actual crystallization pressures when calculated with the barometer for eclogitic compositions after Wijbrands et al. 2016). The coexisting shock-induced mineral grains in the original dense liquids may be formed at similar *P*–*T* conditions. Temperature estimates were done according to the experimentally determined stability fields of lawsonite in the CASH-system (Schmidt 1995) and in the hydrous MORB system (Poli and Schmidt 1995; Okamoto and Maruyama 1999).

Formation pressures of the liebermannite-albitic jadeite-kokchetavite-bearing paragenesis lies in the range of 8.9 – 11.4 GPa as can be estimated from chemical analyses of MajGrt 4 grain (Figs. 10e and 11a; Table 3). Majoritic garnet 5 located between a grossular + vuagnatite zone and a large grain of majorized hornblende and fine-grained chlorite (Figs. 9a and 10f) yielded calculated pressure values between 8.2 and 8.7 GPa (Fig. 11b; Table 3). As can be seen from this figure, the upper temperature limit of stable lawsonite + coesite lies within the stability field of lawsonite in the CASH system but is probably somewhat higher than the upper stability limit of Lws in the system MORB + H_2O.

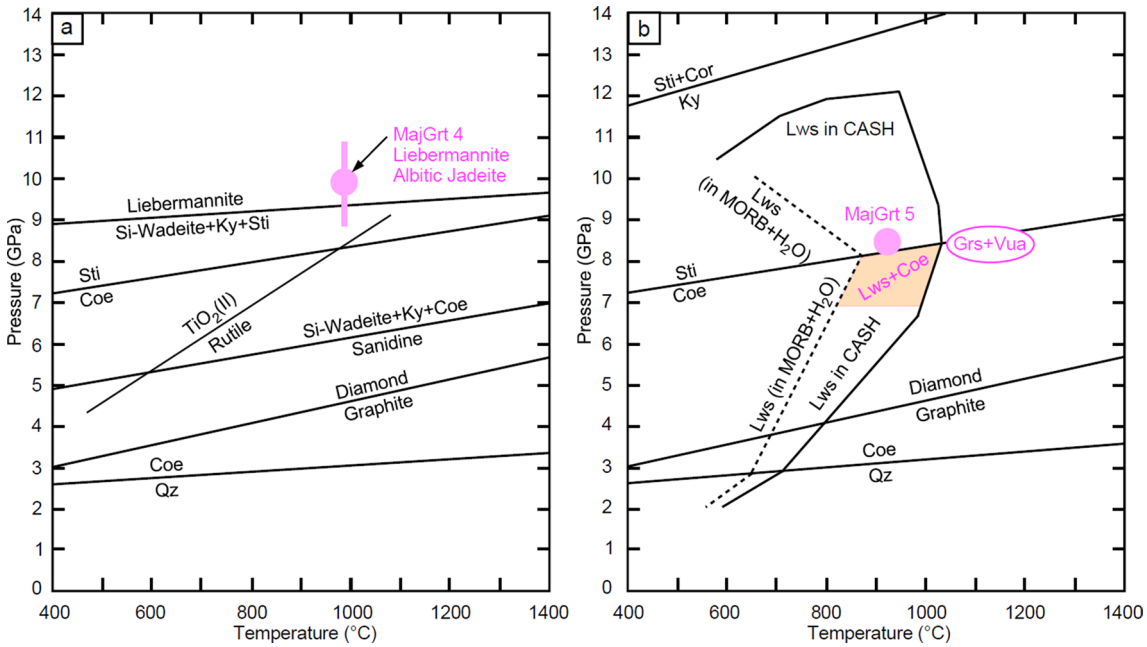

Fig. 11 **a** *P*–*T* diagram with the reactions of liebermannite = Si-wadeite + kyanite + stishovite and Si-wadeite + kyanite + stishovite = sanidine (Chang et al. 2013), Stishovite = Coesite (Ono et al. 2017), Coesite = Quartz (Bose and Gangly 1995), TiO_2 (II) = Rutile (Withers et al. 2003), and Diamond = Graphite (Day 2012). The approximate stability of MajGrt 4 with liebermannite and albitic jadeite is indicated. Note that the exact temperature of this paragenesis is not known. **b** *P*–*T* diagram with stability fields of lawsonite in the CaO-Al_2O_3-SiO_2-H_2O (CASH) system (Schmidt 1995; Poli and Schmidt 1995) and in the system MORB + H_2O (Okamoto and Maruyama 1999). The stability pressure MajGrt 5 is indicated (*T* is assumed). The possible stability of grossular + vuagnatite occurring near to SMVs is indicated

It is obvious from Fig. 11a, b that the crystallization of the shock-induced phases liebermannite, albitic jadeite, kokchetavite, vuagnatite and lawsonite + coesite started at ~ 900 °C in the low-pressure part of the stability field of liebermannite and continued to the high-pressure part of the lawsonite + coesite stability fields.

P–T evolution after shock-melt vein generation

The investigated coarse-grained amphibolite clasts contain SMVs that are thin relative to the average mineral grain size. Moreover, the rocks contain secondary 'pre-Ries' veinlets consisting of either prehnite or analcime, and many of their Ca-rich plagioclase grains were severely sericitized before the impact. These conditions lead to different chemical bulk compositions of both the SMVs and their neighborhoods. Therefore, it is important to take into consideration local equilibrium values and reactive bulk compositions. Another important aspect lies in the maximum *P–T* conditions that were reached in both the SMVs and their surrounding areas within distances of about 300 µm to the SMV. Still, there is another fact that needs to be mentioned and this is the role of H_2O during metamorphic mineral formation. Water always makes easier and faster metamorphic reactions, no matter of which kind these reactions are. Another quite important point is the rheological character of the target rock. In this respect, a massive amphibolite is completely different from a chondrite.

After the generation of shock-melt veins (SMV) at ~ 17 GPa and 2100 °C (Fig. 12), rapid cooling occurred resulting in MajGrt 1 crystallization that was sometimes accompanied by precipitation of stishovite (Stähle et al. 2011, 2017). Somewhat lower pressures of ~ 16.3 GPa are indicated by MajGrt 2 that occurs just outside the SMVs and is generally embedded in a montmorillonite matrix interpreted to result from former melt glass (Fig. 10b–d). Temperatures are thought to have been considerably lower than those during the growth of MajGrt 1, because there are no signs of retrogression (Fig. 12). A grain of magnesio-hornblende still further away from the SMV and MajGrt 2 (Fig. 10b), shows a thin garnetiferous seam of MajGrt 3 that was produced at considerably lower pressure of ~ 13.3 GPa.

Since for the Ries impact a rather short isobaric shock pulse of ~ 20 ms should be envisaged (Stähle et al. 2017) and SMVs are relatively thin, it can be assumed that quenching occurred already during this shock pulse (at least in the interior parts of the SMV) and followed a rather steep and near-isobaric cooling *P–T* path, whereby the extent of isobaric cooling is inversely related to the amount of melt being cooled by conduction. This part of the cooling path would then be followed by a phase of decompression with reduced cooling (Hu and Sharp 2022), making the path flatter in a *T-P* diagram (Fig. 12).

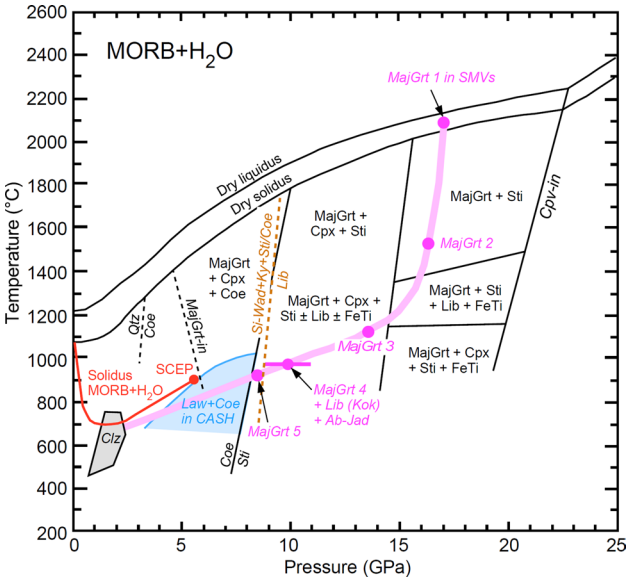

Fig. 12 *T-P* phase diagram for MORB based on experimental data of Litasov and Ohtani (2005). For the sake of clarity, data above about 20 GPa have been omitted, because they are not relevant for this study. In addition to this phase diagram, stability limits for clinozoisite (Wei and Zheng 2020), lawsonite + coesite (Okamoto and Maruyama 1999) and phengite (Schmidt and Poli 1998) in the MORB + H_2O system are given. Moreover, the MajGrt-in boundary was taken from van Roermund et al. (2000), the Qtz/Coe phase boundary from Bose and Ganguly (1995), and the reaction boundary between Si-wadeite + Ky + Sti/Coe = liebermannite (Lib) from Akaogi et al. (2004) and Chen et al. (2019). Furthermore, the solidus of MORB + H_2O with its second critical end point (SCEP) is from Schmidt and Poli (1998). Our study is primarily based on magmatic and metamorphic minerals from SMVs and their immediate neighborhood (< 320 µm away from the SMV boundaries). Shock-produced phases are five different textural types of majoritic garnets that were found either within SMVs (MajGrt 1) or outside SMVs with increasing distances from their rims (MajGrt 2 to 5). All these texturally different majoritic garnets only provide *P* estimates, but temperatures are subject to considerable uncertainty

The occurrence of liebermannite, kokchetavite and albitic jadeite in the immediate vicinity of MajGrt 4 (Fig. 10e) indicates crystallization pressures of nearly 10 GPa (Fig. 11a). At still somewhat lower pressures between 9 and 8 GPa, MajGrt 5 was formed (Figs. 9a, 10f). This majoritic garnet was generated at *P–T* conditions lower than those of the zone that is ruled by grossular and vuagnatite, but higher than those of the stability field of lawsonite + coesite in MORB compositions (Fig. 11b). Finally, there is a low-pressure and -temperature zone of the stability of clinozoisite in MORB compositions after Wei and Zheng (2020). These conditions were only observed in sample ZLN128 at a relatively large distance from the SMV (~ 300 µm). Here, clinozoisite suppresses prehnite (Fig. 4c).

At this stage of discussion, two matters should be taken into consideration. First, majoritic garnets are relatively

good indicators of pressure, particularly when they were formed within melts, such as MajGrt 1, 2, 3 and 5 that all are in contact with former glass (Fig. 10b–d). Even MajGrt 4 was most probably in contact with K-Na-rich melt (Fig. 10e). Temperature values for these majoritic garnets are less clear, but at the beginning of cooling and decompression the shock melt vein is much hotter than the surrounding bulk rock ($\Delta T \approx 1500$ °C). This implies rapid heat transfer into the cold neighborhood of the SMV and rapid quench of SMV phases leading to a relatively steep *P–T* decompression path. Moreover, survival of ultrahigh-*P* phases is only possible, if they cool fast below a critical temperature, before a significant pressure release takes place (Hu and Sharp 2022). In our case, the areal distribution of mineral zones with increasing distance from the SMVs mimics the stability fields of the observed phases and thus clearly shows first a temperature decrease and then a significant pressure release.

Conclusions

Shock-induced melt veins in meteorites or terrestrial impactites are local hot zones with high-temperature values of > 2000 °C. The melt veins in the Ries crater are predominantly restricted to moderately shocked rocks (stages M-S3 to M-S4) with otherwise completely intact primary textures. However, in suevites of the Ries, within stronger shocked rocks with pumice-like textures (stage F-S6) any shock veins are apparently lacking. Unlike most meteorites, the investigated amphibolites were dense silicate rocks.

The creation of local melts along and outside the walls of shock veins was mainly favored by low melting points of hydrothermal OH-bearing minerals (analcime, prehnite, chlorite) or hornblende, and casually with localized supply of H_2O from sericitized plagioclase. During shock pressure release, intermixtures of variable mineral melts and mafic melts may cause formation of stoichiometric and nonstoichiometric jadeite. Fused prehnite induces crystallization of clinozoisite. Melts of Na-rich plagioclase with sericite fillings gave cause for the formation of liebermannite, albitic jadeite, kokchetavite and phengite. Plagioclase ($An_{71–75}$) with local supply of H_2O is responsible for the creation of grossular, vuagnatite + grossular, vuagnatite, and lawsonite + coesite.

Local melts that formed outside of the shock veins occur at maximum distances of ~ 300 µm from the edges of these veins. The newly observed high-pressure phases therein show the following characteristics:

1. Chemical composition of majoritic garnet 4 and 5 in local melts at the walls indicate high pressures in the range of ~ 8.4–11.4 GPa. The occurrence of lawsonite + coesite assemblages adjacent to the shock veins restrict the maximal operating temperatures to somewhat less than 1030 °C.
2. The occurrence of liebermannite within a sericitized clast of DPG and in local melts adjacent to shock veins could be ascertained by usage of Raman spectroscopy. The occurrence of this dense high-pressure polymorph with sixfold coordinated Si was verified for the first time in the Ries impact structure.
3. Albitic jadeite with a vacancy at the M2 site of ~ 0.23 apfu is a Si-rich Na-pyroxene (Si ≈ 2.20 apfu) that very probably substitutes for jadeite + coesite/stishovite in the shock-induced high-pressure melts.
4. Vuagnatite with the chemical formula $CaAl[SiO_4](OH)$ and a calculated density of 3.416 g/cm^3 actually is a high-pressure phase. The occurrence of this phase in shocked Ries rocks confirms a long-standing prediction. Vuagnatite in amphibolite ZLN128a grew within shock-induced melts of plagioclase composition. However, its stability in the *P–T* field is not known.
5. Kokchetavite ($KAlSi_3O_8$) occurs as single phase or together with liebermannite and albitic jadeite in alkali-rich melt glasses. It is a stable phase at lower pressures (< 3 GPa) and was now identified in shocked rocks of the Ries.
6. Phengite and clinozoisite are high-pressure phases that occur occasionally in alkali-rich or alkali-calcium-rich melt glasses. Fine-grained aggregates of lawsonite and coesite were formed from An-rich plagioclase under simultaneous influx of H_2O-rich solutions.

Finally, it should be mentioned that many shock features found in basaltic achondrites like Martian meteorite Zagami are also present in veined amphibolites from the Ries impact crater. We also suppose that terrestrial shocked rocks of diverse chemical compositions and with hydrous minerals may contain many new high-pressure phases, provided that water-bearing melts are produced. It should be emphasized that growth, spatial occurrence and chemical composition of the shock-induced high-pressure phases within and adjacent SMVs retain a multitude of physical data of the transient, high-speed shock wave that was ultimately created by an asteroid impact.

Acknowledgements Our thanks are due to Ilona Fin and Oliver Wienand for preparing excellent polished thin sections and to Johannes Grimm and Hans-Peter Meyer for their assistance with EMPA analyses. Manuela Zeug is thanked for carrying out some analyses with micro-Raman spectroscopy. Careful reviews by Othmar Müntener and two anonymous reviewers are gratefully acknowledged.

Funding Open Access funding enabled and organized by Projekt DEAL. We thank Klaus Tschira-Stiftung, Heidelberg, for financial support.

Declarations

Conflict of interests The authors have no financial or proprietary interests in any material discussed in this article.

References

Akaogi M, Kamii N, Kishi A, Kojitani H (2004) Calorimetric study on high-pressure transitions in $KAlSi_3O_8$. Phys Chem Minerals 31:85–91. https://doi.org/10.1007/s00269-003-0372-9

Baziotis I, Stamatios X, Papoutsa A, Hu J, Ma C, Klemme S, Berndt J, Ferrière L, Caracas R, Asimow PD (2022) Jadeite and related species in shocked meteorites: Limitations on inference of shock conditions. Am Mineral, in Press. https://doi.org/10.2138/am-2022-8220

Beck P, Gillet P, El Goresy A, Mostefaoui S (2005) Timescales of shock processes in chondritic and Martian meteorites. Nature 435:1071–1074. https://doi.org/10.1038/nature03616

Biren MB, Spray JG (2011) Shock veins in the central uplift of the Manicouagan impact structure: context and genesis. Earth Planet Sci Lett 303:310–322. https://doi.org/10.1016/j.epsl.2011.01.003

Boonsue S, Spray JG (2017) Shock-generated labradorite polymorphs in terrestrial impact rocks at Manicouagan. Lunar Planet Sci 48:2557

Bose K, Ganguly J (1995) Quartz-coesite transition revisited: Reversed experimental determination at 500–1200 °C and retrieved thermochemical properties. Am Mineral 80:231–238

Brockamp O, Schlegel A, Wemmer K (2015) Complex hydrothermal alteration and illite K-Ar ages in Upper Visean molasse sediments and magmatic rocks of the Variscan Badenweiler-Lenzkirch suture zone, Black Forest, Germany. Int J Earth Sci 104:683–702. https://doi.org/10.1007/s00531-014-1118-2

Buchner E, Schmieder M, Schwarz WH, Trieloff M (2013) Das Alter des Meteoritenkraters Nördlinger Ries – eine Übersicht und kurze Diskussion der neueren Datierungen des Riesimpakts. Z Dt Ges Geowiss (german J Geosci) 164:433–445. https://doi.org/10.1127/1860-1804/2013/0037

Chang L, Liu X, Liu H, Kojitani H, Wang S (2013) Vibrational mode analysis and heat capacity calculation of $K_2SiSi_3O_4$-wadeite. Phys Chem Minerals 40:563–574. https://doi.org/10.1007/s00269-013-0593-5

Chao ECT (1967) Shock effects in certain rock-forming minerals. Science 156:192–202

Chao ECT (1968) Pressure and temperature histories of impact metamorphosed rocks–based on petrographic observations. In: French BM, Short NM (eds) Shock metamorphism of natural materials. Mono Book Corp, Baltimore, pp 135–158

Chao ECT, Hüttner R, Schmidt-Kaler H (1978) Principal exposures of the Ries meteorite crater in southern Germany. Bayer Geol Landesamt, München p 84

Chen M, Sharp TG, El Goresy A, Wopenka B, Xie X (1996) The majorite-pyrope + magnesiowüstite assemblage: constraints on the history of shock veins in chondrites. Science 271:1570–1573

Chen T, Gwanmesia GD, Ehm L, Le Losq C, Neuville DR, Phillips BL, Li B, Liebermann RC (2019) Synthesis and characterization of polycrystalline $KAlSi_3O_8$ hollandite [liebermannite]: Sound velocities vs. pressure to 13 GPa at room temperature. C R Geoscience 351:113–120. https://doi.org/10.1016/j.crte.2018.09.009

Collerson KD, Williams Q, Kamber BS, Omori S, Arai H, Ohtani E (2010) Majoritic garnet: A new approach to pressure estimation of shock events in meteorites and the encapsulation of sublithospheric inclusions in diamond. Geochim Cosmochim Acta 74:5939–5957

Craw D, Landis CA, Kawachi Y (1979) Vuagnatite in New Zealand (Note). New Zealand J Geol Geophys 22:627–629

Day HW (2012) A revised diamond-graphite transition curve. Am Mineral 97:52–62

Dressler B, Graup G (1970) Pseudotachylite aus dem Nördlinger Ries. Geol Bavar 61:201–228

Dressler B, Graup G, Matzke K (1969) Die Gesteine des kristallinen Grundgebirges im Nördlinger Ries. Geol Bavar 61:201–228

Ferrero S, Ziemann MA, Angel RJ, O'Brien PJ, Wunder B (2016) Kumdykolite, kokchetavite, and cristobalite crystallized in nanogranites from felsic granulites, Orlica-Snieznik Dome (Bohemian Massif): not evidence for ultrahigh-pressure conditions. Contrib Mineral Petrol 171:3. https://doi.org/10.1007/s00410-015-1220-x

French BM, Koeberl Ch (2010) The convincing identification of terrestrial meteorite impact structures: What works, what doesn't, and why. Earth-Sci Reviews 98:123–170. https://doi.org/10.1016/j.earscirev.2009.10.009

French BM, Short NM (1968) Shock metamorphism of natural materials. Mono Book corporation, Baltimore, p 644

French BM (1998) Traces of Catastrophe: A Handbook of Shock-Metamorphic Effects in Terrestrial Meteorite Impact Structures. LPI Contribution No. 954 Lunar and Planetary Institute, Houston, 120 pp

Gatta GD, Lee Y (2014) Zeolites at high pressure: A review. Mineral Mag 78(2):267–291. https://doi.org/10.1180/minmag.2014.078.2.04

Gatta GD, Nestola F, Boffa Ballaran T (2006) Elastic behavior, phase transition, and pressure induced structural evolution of analcime. Am Mineral 91:568–578. https://doi.org/10.2138/am.2006.1994

Gillet P, Sautter V, Harris J, Reynard B, Harte B, Kunz M (2002) Raman spectroscopic study of garnet inclusions in diamonds from the mantle transition zone. Am Mineral 87:312–317. https://doi.org/10.2138/am-2002-2-313

Gillet P, El Goresy A, Beck P, Chen M (2007) High-pressure mineral assemblages in shocked meteorites and shocked terrestrial rocks: Mechanisms of phase transformations and constraints to pressure and temperature histories. In: Ohtani E (ed) Advances in high-pressure mineralogy. Geol Soc Amer Spec Paper, Boulder, pp 57–82. https://doi.org/10.1130/2007.2421(05)

Graup G (1978) Das Kristallin im Nördlinger Ries – Petrographische Zusammensetzung und Auswurfmechanismus der kristallinen Trümmermassen. Enke Verlag, Stuttgart, Struktur des kristallinen Untergrundes und Beziehungen zum Moldanubikum, p 190

Hawthorne FC, Oberti R, Harlow GE, Maresch WV, Martin RF, Schumacher JC, Welch MD (2012) Nomenclature of the amphibole supergroup. Am Mineral 97:2031–2048. https://doi.org/10.2138/am.2012.4276

Heider N, Kenkmann T (2003) Numerical simulation of temperature effects at fissures due to shock loading. Meteorit Planet Sci 38:1451–1460

Hikosaka K, Sinmyo R, Hirose K, Ishii T, Ohishi Y (2019) The stability of Fe_5O_6 and Fe_4O_5 at high pressure and temperature. Am Mineral 104:1356–1359. https://doi.org/10.2138/am-2019-7097

Hu J, Sharp TG (2022) Formation, preservation and extinction of high-pressure minerals in meteorites: temperature effects in shock metamorphism and shock classification. Prog Earth Planet Sci 9:6. https://doi.org/10.1186/s40645-021-00463-2

Hüttner R, Schmidt-Kaler H (1999) Meteoritenkrater Nördlinger Ries. Wanderungen in der Erdgeschichte 10:1–144

Hwang S-L, Shen P, Chu H-T, Yui T-F, Liou JG, Sobolev NV, Zhang R-Y, Shatsky VS (2004) Kokchetavite: a new potassium-feldspar polymorph from the Kokchetav ultrahigh-pressure terrane. Contrib Mineral Petrol 148:380–389. https://doi.org/10.1007/s00410-004-0610-2

James OB (1969) Jadeite: Shock-induced formation from oligoclase, Ries Crater, Germany. Science 165:1005–1008

Jaret SJ, Woerner WR, Phillips BL, Ehm L, Nekvasil H, Wright SP, Glotch TD (2015) Maskelynite formation via solid-state transformation: Evidence of infrared and X-ray anisotropy. J Geophys Res Planets 120:570–587. https://doi.org/10.1002/2014JE004764

Kanzaki M, Xue X, Amalberti J, Zhang Q (2012) Raman and NMR spectroscopic characterization of high-pressure K-cymrite ($KAlSi_3O_8{\cdot}H_2O$) and its anhydrous form (kokchetavite). J Mineral Petrol Sci 107:114–119 https://doi.org/10.2465/jmps.111020i

Kenkmann T, Hornemann U, Stöffler D (2000) Experimental generation of shock-induced pseudotachylites along lithological interfaces. Meteorit Planet Sci 35:1275–1290

Kunz M, Gillet P, Fiquet G, Sautter V, Graafsma H, Conrad P, Harris J (2002) Combined in situ X-ray diffraction and Raman spectroscopy on majorite garnet inclusions in diamonds. Earth Planet Sci Lett 198:485–493

Langenhorst F (2002) Shock metamorphism of some minerals: Basic introduction and microstructural observations. Bull Czech Geol Survey 77:265–282

Langenhorst F, Deutsch A (2012) Shock metamorphism of minerals. Elements 8:31–36. https://doi.org/10.2113/gselements.8.1.31

Langenhorst F, Poirier JP (2000a) 'Eclogitic' minerals in a shocked basaltic meteorite. Earth Planet Sci Lett 176:259–265

Langenhorst F, Poirier JP (2000b) Anatomy of black veins in Zagami: clues to the formation of high-pressure phases. Earth Planet Sci Lett 184:37–55

Lavina B, Meng Y (2015) Unraveling the complexity of iron oxides at high pressure and temperature: synthesis of Fe_5O_6. Sci Adv 1(5):e1400260. https://doi.org/10.1126/sciadv.1400260

Lavina B, Dera P, Kim E, Meng Y, Downs RT, Weck PF, Sutton SR, Zhao Y (2011) Discovery of the recoverable high-pressure iron oxide Fe_4O_5. PNAS 108:17281–17285. https://doi.org/10.1073/pnas.1107573108

Li H, Zhang F, Christy AG (2011) The correlation between Raman spectra and the mineral composition of muscovite and phengite. In: Dobrzhinetskaya LF, Faryad SW, Wallis S, Cuthbert S (eds) Ultrahigh-pressure metamorphism – 25 Years after the discovery of coesite and diamond. Elsevier, Amsterdam, pp 197–212. https://doi.org/10.1016/B978-0-12-385144-4.00006-0

Likhacheva AY, Rashchenko SV, Seryotkin YV (2012) The deformation mechanism of a pressure-induced phase transition in dehydrated analcime. Mineral Mag 76:129–142. https://doi.org/10.1180/minmag.2012.076.1.129

Lippolt HJ, Kirsch H (1994) Isotopic investigation of post-Variscan plagioclase sericitization in the Schwarzwald gneiss massif. Chem Erde 54:179–198

Litasov KD, Ohtani E (2005) Phase relations in hydrous MORB at 18–28 GPa: implications for heterogeneity of the lower mantle. Phys Earth Planet Int 150:239–263. https://doi.org/10.1016/j.pepi.2004.10.010

Liu L-G, Lin C-C, Yung YJ, Mernagh TP, Irifune T (2009) Raman spectroscopic study of K-lingunite at various pressures and temperatures. Phys Chem Minerals 36:143–149. https://doi.org/10.1007/s00269-008-0264-0

Liu X, Ohfuji H, Nishiyama N, He Q, Sanehira T, Irifune T (2012) High-P behavior of anorthite composition and some phase relations of CaO-Al_2O_3-SiO_2 system to the lower mantle of the Earth, and their geophysical implications. J Geophys Res 117:09205. https://doi.org/10.1029/2012/2012JB009290,2012

Ma C, Tschauner O, Beckett JR, Liu Y, Rossman GR, Sinogeikin SV, Smith JS, Tayloer LA (2016) Ahrensite, γ-Fe_2SiO_4, a new shock-metamorphic mineral from the Tissint meteorite: Implications for the Tissint shock event on Mars. Geochim Cosmochim Acta 184:240–256. https://doi.org/10.1016/j.gca.2016.04.042

Ma C, Tschauner O, Beckett JR, Rossman GR, Prescher C, Prakapenka VB, Bechtel HA, MacDowell A (2018) Liebermannite, $KAlSi_3O_8$, a new shock-metamorphic, high-pressure mineral from the Zagami Martian meteorite. Meteorit Planet Sci 53:50–61. https://doi.org/10.1111/maps.13000

Ma C, Tschauner O, Kong M, Beckett JR, Greenberg E, Prakapenka VB, Lee Y (2022) A high-pressure, clinopyroxene-structured polymorph of albite in highly shocked terrestrial and meteoritic rocks. Am Mineral 107:625–630. https://doi.org/10.2138/am-2021-7925

Ma C, Tschauner O, Kong M, Beckett JR, Greenberg E, Prakapenka VB, Lee Y (2020) Discovery of a highly-defective, shock-induced, high-pressure albitic jadeite, $(Na,Ca,\square_{1/4})(Al,Si)Si_2O_6$: Natural occurrence of a clinopyroxene with excess Si. 51st Lunar Planet Sci Conf, #1712.pdf

Martini JEJ (1978) Coesite and stishovite in the Vredefort Dome, South Africa. Nature 272:715–717

Martini JEJ (1991) The nature, distribution and genesis of the coesite and stishovite associated with pseudotachylite of the Vredefort Dome, South Africa. Earth Planet Sci Lett 103:285–300

Matsubara S, Kato A, Sakurai K (1977) The occurrence of vuagnatite from Shiraki, Toba, Mie Prefecture, Japan. Bull Natn Sci Mus C 3:41–48

Mc Near E, Vincent MG, Parthé E (1976) The crystal structure of vuagnatite, $CaAl(OH)SiO_4$. Am Mineral 61:831–838

McCormick TC (1986) Crystal-chemical aspects of nonstoichiometric pyroxenes. Am Mineral 71:1434–1440

Melosh HJ (1989) Impact cratering: A Geologic Process. Oxford Univ, New York, p 245

Melosh HJ (2013) The contact and compression stage of impact cratering. In: Osinski GR, Pierazzo E (eds) Impact cratering processes and products. Blackwell, West Lafayette, pp 32–42

Mikhno AO, Schmidt U, Korsakov AV (2013) Origin of K-cymrite and kokchetavite in the polyphase mineral inclusions from Kokchetav UHP calcsilicate rocks: evidence from confocal Raman imaging. Eur J Mineral 25:807–816. https://doi.org/10.1127/0935-1221/2013/0025-2321

Miyahara M, Tomioka N, Bindi L (2021) Natural and experimental high-pressure, shock-produced terrestrial and extraterrestrial materials. Prog Earth Planet Sci 8:59. https://doi.org/10.1186/s40645-021-00451-6

Myhill R, Ojwang DO, Ziberna L, Frost DJ, Boffa Ballaran T, Miyahama N (2016) On the P-T-fO_2 stability of Fe_4O_5, Fe_5O_6 and Fe_4O_5-rich solid solutions. Contrib Mineral Petrol 171:51. https://doi.org/10.1007/s00410-016-1258-4

Nasdala L, Akhmadaliev S, Artac A, Chanmuang NC, Habler G, Lenz C (2018) Irradiation effects in monazite-(Ce) and zircon: Raman and photoluminescence study of Au-irradiated FIB

foils. Phys Chem Minerals 45:855–871. https://doi.org/10.1007/s00269-018-0975-9
Nishiyama N, Rapp RP, Irifune T, Sanehira T, Yamazaki D, Funakoshi K (2005) Stability and *P-V-T* equation of state of $KAlSi_3O_8$-hollandite determined by in situ X-ray observations and implications for dynamics of subducted continental crust material. Phys Chem Minerals 32:627–637. https://doi.org/10.1007/s00269-005-0037-y
Ogilvie P, Gibson RL, Reimold WU, Deutsch A, Hornemann U (2011) Experimental investigation of shock metamorphic effects in a metapelitic granulite: The importance of shock impedance contrast between components. Meteorit Planet Sci 46:1565–1586. https://doi.org/10.1111/j.1945-5100.2011.01250.x
Ohtani E, Kimura Y, Kimura M, Takata T, Kondo T, Kubo T (2004) Formation of high-pressure minerals in shocked L6 chondrite Yamato 791384: constraints on shock conditions and parent body size. Earth Planet Sci Lett 227:505–515. https://doi.org/10.1016/j.epsl.2004.08.018
Okamoto K, Maruyama S (1999) The high-pressure synthesis of lawsonite in the MORB+H_2O system. Am Mineral 84:362–373
Ono S, Kikegawa T, Higo Y, Tange Y (2017) Precise determination of the phase boundary between coesite and stishovite in SiO_2. Phys Earth Planet Int 264:1–6. https://doi.org/10.1016/j.pepi.2017.01.003
Ono S (1998) Stability limits of hydrous minerals in sediment and mid-ocean ridge basalt compositions: Implications for water transport in subduction zones. J Geophy Res 103:18,253–18,267
Pabst A (1977) Über einige dichte, wasserhaltige Calcium- bzw. Barium-Silikate aus der Franciscan-Formation, California (Lawsonit, Vuagnatit, Rosenhahnit, Cymrit). N Jb Mineral Abh 129:1–14
Pohl J, Stöffler D, Gall H, Ernstson K (1977) The Ries impact crater. In: Roddy DJ, Pepin RO, Merill RB (eds) Impact and explosion cratering. Pergamon Press, New York, pp 343–404
Poli S, Schmidt MW (1995) H_2O transport and release in subduction zones: Experimental constraints on basaltic and andesitic systems. J Geophys Res 100:22,299-22,314
Poli S, Schmidt MW (2002) Petrology of subducted slabs. Annu Rev Earth Planet Sci 30:207–235. https://doi.org/10.1146/annurev.earth.30.091201.140550
Prencipe M, Maschio L, Kirtman B, Salustro S, Erba A, Dovesi R (2014) Raman spectrum of $NaAlSi_2O_6$ jadeite. A quantum mechanical simulation. J Raman Spectrosc 45:703–709. https://doi.org/10.1002/jrs.4519
Ringwood AE, Reid AF, Wadsley AD (1967) High-pressure $KAlSi_3O_8$, an aluminosilicate with sixfold coordination. Acta Cryst 23:1093–1095
Robertson PB, Dence MR, Vos MA (1968) Deformation in rock-forming minerals from Canadian Craters. In: French BM, Short NM (eds) Shock metamorphism of natural materials. Mono Book Corp, Baltimore, pp 433–452
Romanenko AV, Rashchenko SV, Sokol AG, Korsakov AV, Seryotkin YV, Glazyrin KV, Musiyachenko K (2021) Am Mineral 106:404–409. https://doi.org/10.2138/am-2020-7407
Sarp H, Bertrand J, Mc Near E (1976) Vuagnatite, $CaAl(OH)SiO_4$, a new natural calcium aluminium nesosilicate. Am Mineral 61:825–830
Schlegel A, Brockamp O, Clauer N (2007) Response of clastic sediments to episodic hydrothermal fluid flows in intramontane troughs: a case study from Black Forest, Germany. Eur J Mineral 19:833–848. https://doi.org/10.1127/0935-1221/2007/0019-1768
Schmidt MW (1995) Lawsonite: Upper pressure stability and formation of higher density hydrous phases. Am Mineral 80:1286–1292
Schmidt MW, Poli S (1998) Experimentally based water budgets for dehydrating slabs and consequences for arc magma generation. Earth Planet Sci Lett 163:361–379
Schmidt-Kaler H, Treibs W, Hüttner R (1970) Exkursionsführer zur geologischen Übersichtskarte des Rieses, 1:100,000. Bayer Geol Landesamt, München, p 68
Schmieder M, Kennedy T, Jourdan F, Buchner E, Reimold UW (2018) A high-precision $^{40}Ar/^{39}Ar$ age for the Nördlinger Ries impact crater, Germany, and implications for the accurate dating of terrestrial impact events. Geochim Cosmochim Acta 220:146–157. https://doi.org/10.1016/j.gca.2017.09.036
Schwarz WH, Lippolt HJ (2014) ^{40}Ar-^{39}Ar step-heating of impact glasses from the Nördlinger Ries impact crater – Implications on excess argon in impact melts and tektites. Meteor Planet Sci 49:1023–1036. https://doi.org/10.1111/maps12309
Schwarz WH, Hanel M, Trieloff M (2020) U-Pb dating of zircons from an impact melt from the Nördlinger Ries crater. Meteor Planet Sci 55:312–325. https://doi.org/10.1111/maps.13437
Sharp TG, DeCarli PS (2006) Shock effects in meteorites. In: Lauretta DS, McSween HY (eds) Meteorites and the early solar system II. University Arizona Press, Tucson, pp 653–677
Sharp TG, Walton EL, Hu J, Agee C (2019) Shock conditions recorded in NWA 8159 martian augite basalt with implications for the impact cratering history on Mars. Geochim Cosmochim Acta 246:197–212. https://doi.org/10.1016/j.gca.2018.11.014
Spray JG (2010) Frictional melting processes in planetary materials. From hypervelocity impact to earthquakes. Annu Rev Earth Planet Sci 38:221–254. https://doi.org/10.1146/annurev.earth.031208.100045
Spray JG, Boonsue S (2018) Quartz-coesite-stishovite relations in shocked metaquartzites from the Vredefort Impact structure, South Africa. Meteorit Planet Sci 53:93–109. https://doi.org/10.1111/maps.12997
Stähle V, Altherr R, Nasdala L, Ludwig T (2011) Ca-rich majorite derived from high-temperature melt and thermally stressed hornblende in shock veins of crustal rocks from the Ries impact crater (Germany). Contrib Mineral Petrol 161:275–291. https://doi.org/10.1007/s00410-010-0531-1
Stähle V, Altherr R, Nasdala L, Trieloff M, Varychev A (2017) Majoritic garnet grains within shock-induced melt veins in amphibolites from the Ries impact crater suggest ultrahigh crystallization pressures between 18 and 9 GPa. Contrib Mineral Petrol 172:86. https://doi.org/10.1007/s00410-017-1404-7
Stöffler D (1972) Deformation and transformation of rock-forming minerals by natural and experimental shock processes, I. Behavior of minerals under shock compression. Fortschr Mineral 49:50–113
Stöffler D, Grieve RAF (2007) Impactites. In: Fettes D, Desmons J (eds) Metamorphic rocks: a classification and glossary of terms, Recommendations of the International Union of Geological Sciences. Cambridge University Press, Cambridge, Subcommission on the Systematics of Metamorphic Rocks, pp 82–92
Stöffler D, Keil K, Scott ERD (1991) Shock metamorphism of ordinary chondrites. Geochim Cosmochim Acta 55:3845–3867
Stöffler D, Artemieva NA, Wünnemann K, Reimold WU, Jacob J, Hansen BK, Summerson IAT (2013) Ries crater and suevite revisited – observations and modeling. Part I: Observations Meteorit Planet Sci 48:515–589. https://doi.org/10.1111/maps.12086
Stöffler D, Hamann Ch, Metzler K (2018) Shock metamorphism of planetary silicate rocks and sediments: Proposal for an updated classification system. Meteorit Planet Sci 53:5–49. https://doi.org/10.1111/maps.12912
Thompson LM, Spray JG (1996) Pseudotachylite petrogenesis: constraints from the Sudbury impact structure. Contrib Mineral Petrol 125:359–374

Tomioka N, Miyahara M (2017) High-pressure minerals in shocked meteorites. Meteor Planet Sci 52:2017–2039. https://doi.org/10.1111/maps.12902

Tschauner O, Ma C, Beckett JR, Prescher C, Prakapenka VB, Rossman GR (2014) Discovery of bridgmanite, the most abundatnt mineral in Earth, in a shocked meteorite. Science 346:1100–1102. https://doi.org/10.1126/science.1259369

Tschauner O, Ma C, Lanzirotti A, Newville MG (2020a) Riesite, a new high-pressure polymorph of TiO_2 from the Ries impact structure. Minerals 10:78. https://doi.org/10.3390/min10010078

Tschauner O, Ma C, Newville MG, Lanzirotti A (2020b) Structure analysis of natural Wangdaodeite – $LiNbO_3$-type $FeTiO_3$. Minerals 10:1072. https://doi.org/10.3390/min10121072

Urakawa S, Kondo T, Igawa N, Shimomura O, Ohno H (1994) Synchrotron radiation study on the high-pressure and high-temperature phase relations of $KAlSi_3O_8$. Phys Chem Miner 21:387–391

Van Roermund HLM, Drury MR, Barnhoorn A, De Ronde A (2000) Non-silicate inclusions in garnet from an ultra-deep orogenic peridotite. Geol J 35:209–229

Von Engelhardt W, Stöffler D (1968) Stages of shock metamorphism in the crystalline rocks of the Ries basin, Germany. In: French BM, Short NM (eds) Shock metamorphism of natural materials. Mono Book Corp, Baltimore, pp 135–158

Von Engelhardt W (1997) Suevite breccia of the Ries impact crater, Germany: petrography, chemistry and shock metamorphism of crystalline rock clasts. Meteor Plant Sci 32:545–554

Von Engelhardt W, Arndt J, Stöffler D, Müller WF, Jeziorkowski H, Gubser RA (1967) Diaplektische Gläser in den Breccien des Ries von Nördlingen als Anzeichen für Stoßwellenmetamorphose. Contrib Mineral Petrol 15:93–102

Walton EL, Sharp TG, Hu J (2016) Frictional melting processes and the generation of shock veins in terrestrial impact structures: Evidence from the Steen River impact structure, Alberta, Canada. Geochim Cosmochim Acta 180:256–270. https://doi.org/10.1016/j.gca.2016.02.024

Walton EL, Sharp TG, Hu J, Tschauner O (2018) Investigating the response of biotite to impact metamorphism: Examples from the Steen River impact structure, Canada. Meteor Planet Sci 53:75–92. https://doi.org/10.1111/maps.13011

Wang A, Jolliff BL, Haskin LA, Kuebler KE, Viskuvic KM (2001) Characterization and comparison of structural and compositional features of planetary quadrilateral pyroxenes by Raman spectroscopy. Am Mineral 86:790–806

Wei C, Zheng Y (2020) Metamorphism, fluid behavior and magmatism in oceanic subduction zones. Sci China Earth Sci 63(1):52–77. https://doi.org/10.1007/s11430-019-9482-y

Wijbrans CH, Rohrbach A, Klemme S (2016) An experimental investigation of the stability of majoritic garnet in the earth's mantle and an improved majorite geobarometer. Contrib Mineral Petrol 171:50. https://doi.org/10.1007/s00410-016-1255-7

Withers AC, Essene EJ, Zhang Y (2003) Rutile/TiO_2II phase equilibria. Contrib Mineral Petrol 145:199–204. https://doi.org/10.1007/s00410-003-0445-2

Woodland AB, Uenver-Thiele L, Boffa-Ballaran T, Miyajima N, Rosbach K, Ishii T (2022) Stability of Fe_5O_6 and its relation to other Fe-Mg-oxides at high pressures and temperatures. Ame Mineral, in Press. https://doi.org/10.2138/am-2022-8370

Xie Z, Sharp TG, DeCarli PS (2006) High-pressure phases in a shock-induced melt vein of the Tenham L6 chondrite: Constraints on shock pressure and duration. Geochim Cosmochim Acta 70:504–515. https://doi.org/10.1016/j.gca.2005.09.003

Yagi A, Suzuki T, Akaogi M (1994) High pressure transitions in the system $KAlSi_3O_8$-$NaAlSi_3O_8$. Phys Chem Minerals 21:12–17

Yong W, Dachs E, Withers AC, Essene EJ (2006) Heat capacity and phase equilibria of wadeite-type $K_2Si_4O_9$. Contrib Mineral Petrol 155:137–146. https://doi.org/10.1007/s00410-007-0232-6